

2008

A scanning microscope platform for high resolution nonlinear imaging and laser direct writing

Shuangyang Yang
University of Dayton

Follow this and additional works at: https://ecommons.udayton.edu/graduate_theses

Recommended Citation

Yang, Shuangyang, "A scanning microscope platform for high resolution nonlinear imaging and laser direct writing" (2008). *Graduate Theses and Dissertations*. 6500.
https://ecommons.udayton.edu/graduate_theses/6500

This Thesis is brought to you for free and open access by the Theses and Dissertations at eCommons. It has been accepted for inclusion in Graduate Theses and Dissertations by an authorized administrator of eCommons. For more information, please contact mschlange1@udayton.edu, ecommons@udayton.edu.

**A SCANNING MICROSCOPE PLATFORM FOR
HIGH RESOLUTION NONLINEAR IMAGING
AND LASER DIRECT WRITING**

Thesis

Submitted to

**The School of Engineering of the
UNIVERSITY OF DAYTON**

**in Partial Fulfillment of the Requirements for
The Degree**

Master of Science in Electro-Optics Program

by

Shuangyang Yang

UNIVERSITY OF DAYTON

Dayton, Ohio

December, 2008

A SCANNING MICROSCOPE PLATFORM FOR HIGH RESOLUTION NONLINEAR IMAGING AND LASER DIRECT WRITING

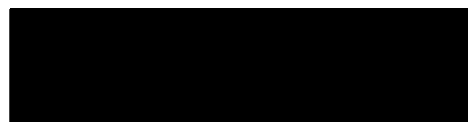
APPROVED BY:



Qiwen Zhan, Ph.D.
Advisory Committee Chairperson
Associate Professor, Electro-Optics
Program
University of Dayton



Peter E. Powers, Ph.D.
Committee Member
Professor, Electro-Optics Program &
Department of Physics
University of Dayton



Joseph W. Haus, Ph.D.
Committee Member
Professor and Director, Electro-Optics
Program
University of Dayton



Malcolm W. Daniels, Ph.D.
Associate Dean
School of Engineering
University of Dayton



Joseph E. Saliba, Ph.D., P.E.
Dean, School of Engineering
University of Dayton

© Copyright by
Shuangyang Yang
All rights reserved
2008

ABSTRACT

A SCANNING MICROSCOPE PLATFORM FOR HIGH RESOLUTION NONLINEAR IMAGING AND LASER DIRECT WRITING

Name: Shuangyang Yang
University of Dayton

Advisor: Dr. Qiwen Zhan and Dr. Peter E. Powers

In this thesis, a scanning microscope platform is built and the instrumentation is described in detail. Two research projects are operated on this platform. The first one is two-photon fluorescence imaging of Titanium dioxide (TiO_2) nano particles with Ruthenium (Ru) metal complex attached inside living A431 cells. A431 cells with nano particles whose size is $30 \sim 50\text{nm}$ inside are inspected under the microscope platform and two-photon fluorescence cell images are generated to probe nano particles with Ru attached inside the living cell. The second project is laser direct writing inside LiNbO_3 with a tightly focused femtosecond laser. Line patterns with widths of several microns can be directly written inside the crystal. The depth of focus can be controlled to have either an elliptical shape with a height of $10 \sim 20\mu\text{m}$ or a round shape with a diameter of only $1 \sim 2\mu\text{m}$ if incident pulse energy and objective lens are carefully chosen. Two defocused optical images are taken to compute the phase profile around the structural modification area using quantitative phase microscopy algorithm. The index difference calculated from the phase profile is -4×10^{-4} . This is a useful characteristic of the structural modification in the crystal.

ACKNOWLEDGEMENTS

My greatest thanks go to my parents, who have been supporting me with their total hearts for more than twenty years. I love them very much but have not had many opportunities to let them know.

I would like to thank my advisors, Dr. Qiwen Zhan and Dr. Peter Powers, for directing my research and providing all necessary equipments. Special thanks are given to the committee members for revising the thesis with patience and expertise.

I want to express my thanks to all the people who have helped this work. It includes Meagan A Roddy from Biology Department who prepares the A431 cells and adds nano particles to cell medium; Dr. Jay Johnson and Elmo A. Blubaugh from UDRI who provide the nano particles.

TABLE OF CONTENTS

CHAPTER

I INTRODUCTION	1
II SCANNING MICROSCOPE PLATFORM OVERVIEW	4
Instrumentation	5
Laser Source	5
Microscope and Stage	6
Spectrometer	6
Photon Detection	6
Labview Development	8
System Initial Tests	10
Two-photon Fluorescence Spectrum Validation	10
Raster Scanning	11
IIITWO-PHOTON FLUORESCENCE IMAGING OF RUTHENIUM	
METAL COMPLEX IN LIVING A431 CELLS	13
Background	13
Nano Particles Preparation	13
System Optimization	14
A431 Cell Preparation	20

Two-photon Fluorescence Imaging of A431 Cells	20
IV LASER DIRECT WRITING INSIDE LINBO₃ CRYSTAL	23
Background	23
System Optimization	29
Structural Modification	30
Measuring Index Change of Structural Modification	31
V SUMMARY AND DISCUSSIONS	34
 APPENDICES	
 A USER MANUAL FOR LABVIEW MASTER PROGRAM	37
NI-Motion Parameters	39
Move Around	40
Nano Stage Output	41
Input & Control Center	42
Counter Parameters & Scope Output	45
Summary	49
 BIBLIOGRAPHY	50

LIST OF FIGURES

II.1	Schematic diagram of scanning microscope platform.	4
II.2	Spectrum of Tsunami laser in mode-locking state around 800nm. . . .	5
II.3	Image of the inverted microscope in use.	7
II.4	A brief flow chart of the whole procedure.	8
II.5	A screenshot of labview program panel.	9
II.6	Comparison of one-photon and two-photon fluorescence spectra of CdS particle sample.	10
II.7	Optical image of SU8 structure on a silicon substrate.	11
II.8	Raster scanning images of SU8 structures on silicon substrate.	12
III.1	The chemical composite of TiO ₂ nano particles with Ru metal complex attached through dopamine.	14
III.2	Two-photon fluorescence intensity versus input laser power of Ru metal complex.	15
III.3	Two-photon fluorescence spectrum of Ru metal complex.	16
III.4	Processed two-photon fluorescence spectra of TiO ₂ particles.	18
III.5	Bar graph showing fluorescence intensity under different excitation wavelength for Ru complex and particles.	19
III.6	A scanning image of cells with particles inside.	21
III.7	Another scanning image of cells with particles inside.	21
III.8	A scanning image of ordinary cells as a comparison.	22

IV.1 Optical image of oil-immersed 630HP fiber under microscope after a 532nm laser line filter.	27
IV.2 Calculated phase profile of 630HP single mode fiber around the core area.	28
IV.3 A scheme of the laser direct writing inside crystal setup. M: mirror; LP: linear polarizer; OL: objective lens; DM: dichroic mirror.	29
IV.4 Elliptical DOF profiles of line patterns inside LiNbO ₃ crystal.	30
IV.5 Round DOF profiles of line patterns inside LiNbO ₃ crystal.	31
IV.6 The DOF profiles of line patterns inside LiNbO ₃ crystal.	32
IV.7 Two defocused optical images of one line pattern inside LiNbO ₃ crystal	32
IV.8 The calculated phase map of a line pattern inside LiNbO ₃ crystal. . .	33
IV.9 A line scan of the calculated phase map of a line pattern inside LiNbO ₃ crystal.	33
A.1 A screenshot of first running front panel of Labview master program.	38
A.2 Figure showing the stage route using 'Generate' function in the 'IN- PUT' section.	43
A.3 A signature made with the labview master program on the surface of LiNbO ₃ by direct laser writing with focused Ti:Sapphire mode-locking beam.	44
A.4 The zigzag scanning route used in raster scanning with SR400 photon counter.	47

LIST OF TABLES

II.1	Characteristics of Tsunami Ti:Sapphire femtosecond laser and Spitfire pro amplifier.	5
II.2	Specifications of the avalanche photodetector.	7

CHAPTER I

INTRODUCTION

In 1873, Ernst Abbe discovered what was to become a well-known paradigm: the inability of a lens-based optical microscope to discern details that are closer together than half of the wavelength of light[1]. When a lens focuses a propagating beam, the light wave interferes constructively at the focal spot and the intensity pattern $I(x, y, z)$ features a main “diffraction” maximum. The full width at half maximum (FWHM) of the spot is given by

$$\Delta r \approx \lambda/(2\text{NA}) \tag{I.1}$$

$$\Delta z \approx n\lambda/\text{NA}^2 \tag{I.2}$$

where λ , n and NA denoting the wavelength, the refractive index and the numerical aperture, respectively.

Since mid-20th century, a lot of efforts have been made to push and break this diffraction limit using various techniques, including multiphoton microscopy(MPM)[2], second and third harmonic generations (SHG,THG)[3, 4], 4Pi microscopy[5], coherent anti-Stokes Raman spectroscopy (CARS)[6], stimulated emission depletion (STED)[7], photoactivatable localization microscopy (PALM)[8] and stochastic optical reconstruction microscopy (STORM)[9]. The optical resolution can reach as high as tens of nanometers.

Among these various microscopy techniques, MPM has become a standard tool for determining the molecular mechanisms of cell-based processes in basic biological research[10], tissue engineering[11] and transgenic mouse models of disease and development[12]. Compared with conventional optical microscopy such as one photon fluorescence or phase contrast microscopy, MPM could provide more detailed molecular and structural information and offer optical sectioning capability for three-dimensional imaging.

Multiphoton excitation is achieved when a molecule simultaneously absorbs two or more low-energy photons, which together provide a total energy sufficient to cause the transition into the excited singlet state. Two-photon excitation(TPE) is the primary signal source since it's the simplest form and easy to operate. If the molecule is fluorescent, it can absorb two excitation photons simultaneously and emit a single photon of fluorescence as if it were excited by a single higher energy photon. This event needs two lower energy photons to interact with the molecule nearly simultaneously($\sim 10^{-16}\text{s}$)[2], resulting in a quadratic dependence on the light intensity instead of linear dependence of conventional fluorescence.

$$I_{\text{fluor}} \propto I_{\text{illum}}^2 \quad (\text{I.3})$$

The intensity squared dependence is the basis of the localized nature of two-photon excitation: doubling the intensity produces four times the fluorescence. It is a typical nonlinear process. The two-photon fluorescence will have a scaled resolution by $\sim \sqrt{2}$.

$$\Delta r \approx \lambda/(\sqrt{8}\text{NA}) \quad (\text{I.4})$$

It is worth to mention another advantage of MPM, which is the ability to preserve the viability of biological samples. The excitation wavelength of one-photon fluorescence is usually within 200nm and 400nm, which lies in the ultraviolet(UV) region. UV light has such a strong energy that most biological samples cannot live under its illumination. However, two-photon excitation uses a wavelength in the visible or infrared region that normally does no harm to the biological samples. Thus MPM provides a method to study *in-vivo* activities in living biological samples.

The two-photon cross-section (σ_{2p}) is a quantitative measure of the probability of a two-photon absorption. σ_{2p} has units of cm^4s , with $10^{-50} \text{ cm}^4\text{s}$ called a Göppert-Mayer or 'GM'. Because it is difficult to measure σ_{2p} directly, the two-photon 'action' cross-section is usually measured; this is the product of the fluorescence quantum yield (ϕ_F) and the absolute two-photon absorption cross-section (σ_{2p})[13].

CHAPTER II

SCANNING MICROSCOPE PLATFORM

OVERVIEW

The schematic diagram of the platform is shown in figure II.1. The linear polarizer and quarter-wave plate generate circularly polarization and act as an isolator to prevent back reflections from interfering with the laser mode-locking state. The filter is carefully chosen to reject the excitation wavelength and pass fluorescence emissions.

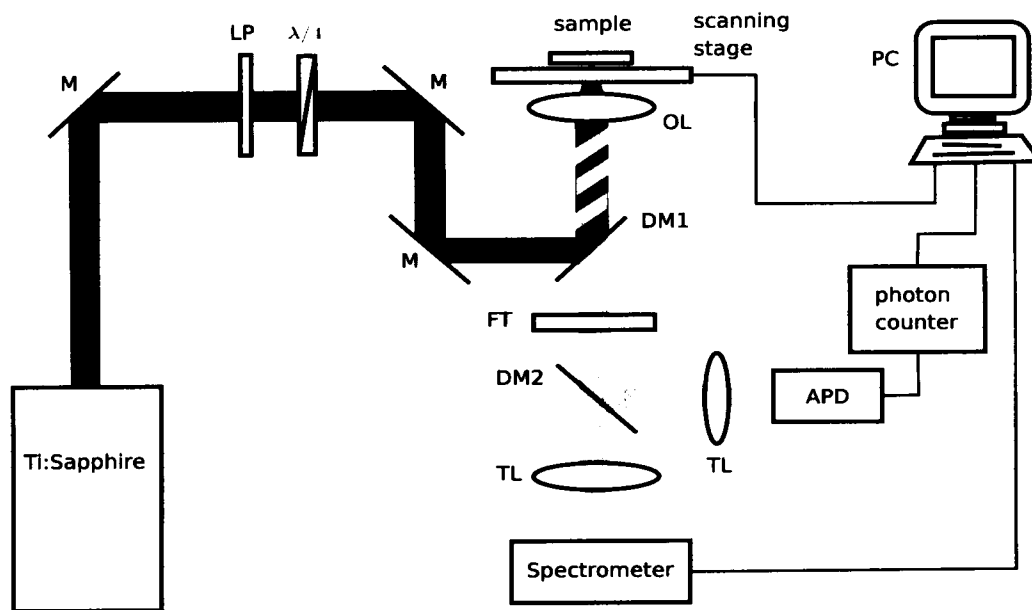


Figure II.1: Schematic diagram of scanning microscope platform. M: mirror; LP: linear polarizer; DM: dichroic mirror; FT: filter; OL: objective lens; TL: tube lens

Instrumentation

Laser Source

The laser source is a Tsunami Ti:Sapphire femtosecond ($10^{-15}s$) laser (Spectra-Physics, Newport) and a Spitfire Pro amplifier (Spectra-Physics, Newport) if higher pulse energy is needed. The specifications are listed in table II.1. The spectrum of the oscillator in mode-locking state is shown in figure II.2, which has a width of 40nm and a central wavelength at 800nm.

Output Characteristics	Tsunami Broadband fs 5W Pump	Spitfire Pro Amplifier
Tuning Range	710-980nm	750-840nm
Average Power	>0.7W at 800nm	>0.7W at 800nm
Pulse Width	<100fs	<120fs
Pulse Energy	~8nJ	>0.2mJ
Repetition Rate	80MHz	5kHz

Table II.1: Characteristics of Tsunami Ti:Sapphire femtosecond laser and Spitfire pro amplifier.

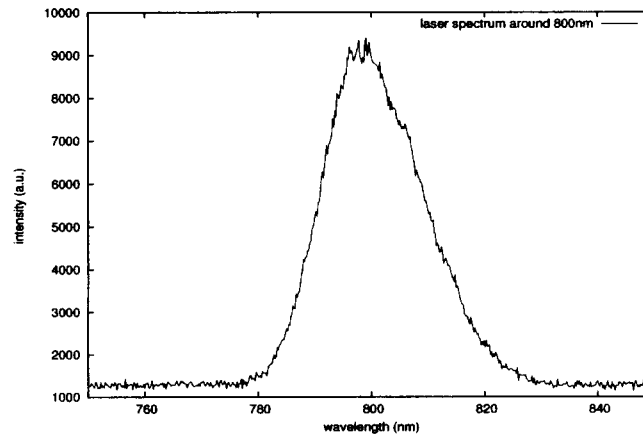


Figure II.2: Spectrum of Tsunami laser in mode-locking state around 800nm.

Microscope and Stage

A Nikon TE2000-U inverted microscope (Nikon, Japan) is the main part in the platform, whose picture is shown in figure II.3. The microscope is infinite conjugated and has several objective lenses to choose from, including an oil-immersed 100x objective lens. The output can be redirected to 5 channels for analysis, including eyepiece and ports on the sides.

An XY microstage (Mad City Labs, WI) is mounted on the microscope, which has a minimum step size of 95.25nm. The objective lens is mounted on a PI z-stage (PI, Germany), which provides a positioning and scanning range of 100 μ m with sub-nanometer resolution and very high linearity. These stages are controlled by labview programs and arbitrary moves can be implemented.

The microscope is equipped with a QICAM Cooled Mono 12-bit CCD camera (QIMAGING, Canada) on the left output channel. It has been calibrated and is controlled by MetaVue imaging software (Molecular Devices, PA) so optical images can be captured and stored.

Spectrometer

The spectrometer in use is USB4000 fiber optics spectrometer (OceanOptics, Florida).

Photon Detection

The detector is an avalanche photodetector (APD) (MPD, Bolzano) with its specification in table II.2. The APD will generate TTL pulses when photons are detected. It is placed right outside the right output channel so the response signals can be collected. The output of the APD is wired to an SR400 gated photon counter (SRS, CA) for counting. The photon counter communicates with Labview programs in a computer

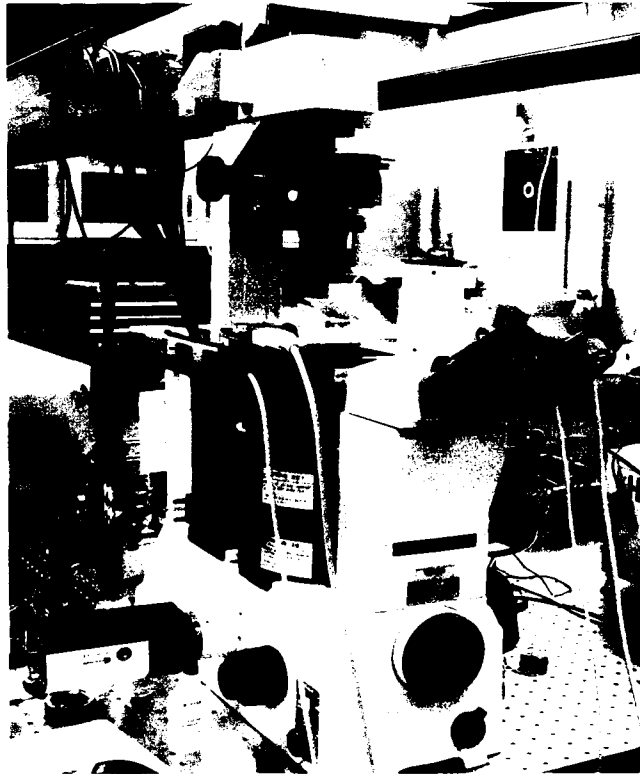


Figure II.3: Image of the inverted microscope in use.

through the GPIB interface.

Sensor Diameter	$50\mu m$ or $100\mu m$
Dark counts	$\sim 10c/s$
Dead time	$77ns$
Maximum count rate	$12.1Mc/s$

Table II.2: Specifications of the avalanche photodetector.

Labview Development

Labview is responsible for device parameters setup, device synchronizations, raster scanning control and data collections. A brief flow chart of the whole procedure is drawn in figure II.4. The details vary upon different samples and applications. A master labview program is developed to handle all the necessary tasks. A screenshot of the front panel is shown in figure II.5. A user manual for this program is specified in APPENDIX A.

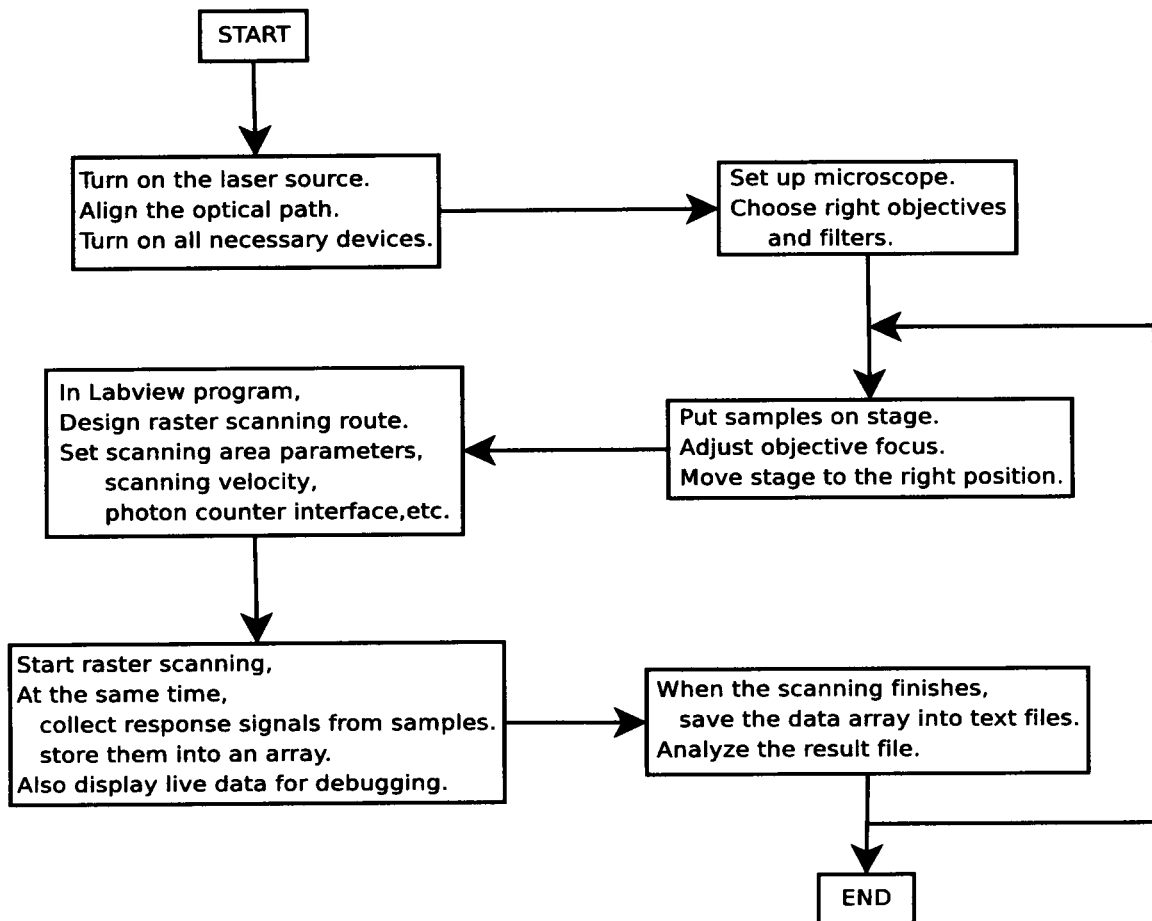


Figure II.4: A brief flow chart of the whole procedure.

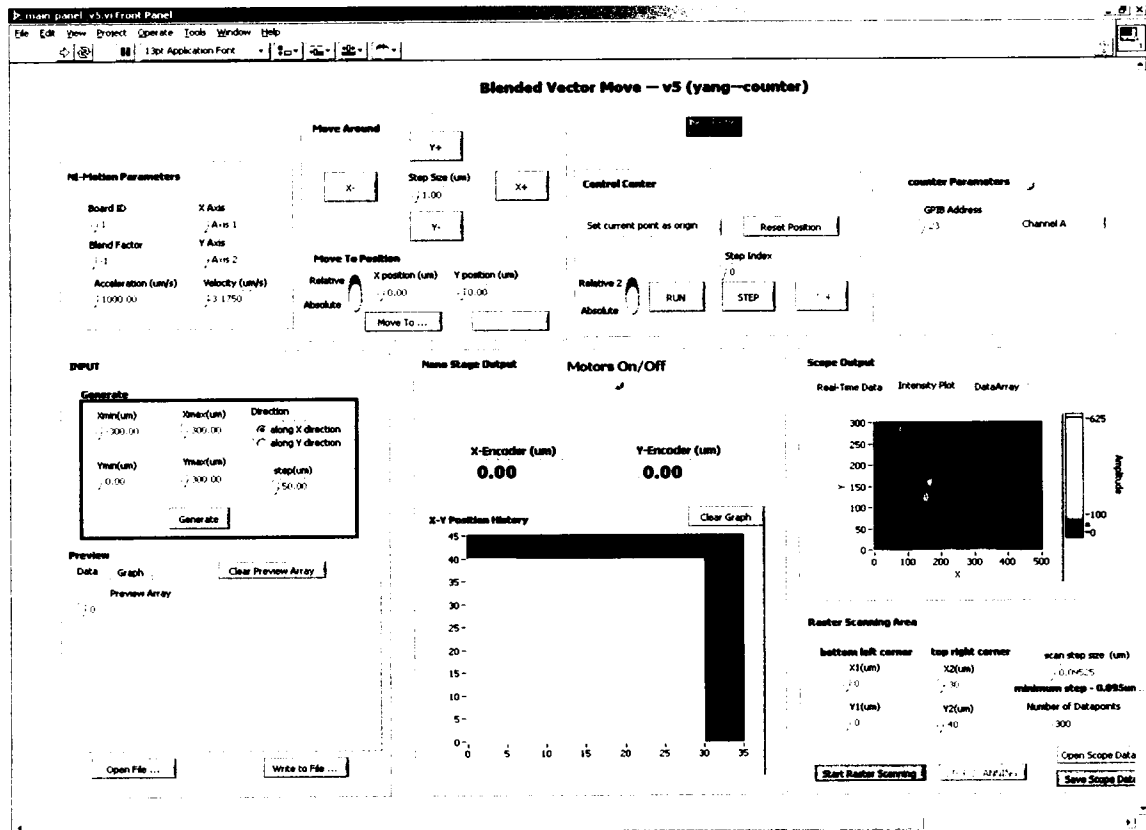


Figure II.5: A screenshot of labview program panel. A user manual is specified in APPENDIX A.

System Initial Tests

Two-photon Fluorescence Spectrum Validation

Two-photon fluorescence of CdS particles sample diluted in solution is investigated to test the whole platform. The sample has a particle size around 10nm . The one-photon fluorescence spectrum is known and is shown in figure II.6(a). The two-photon fluorescence signal from the sample is collected using this system and the analyzed spectrum is shown in figure II.6(b). By comparing these two spectra, the two-photon fluorescence spectrum result is similar to the one-photon fluorescence spectrum result.

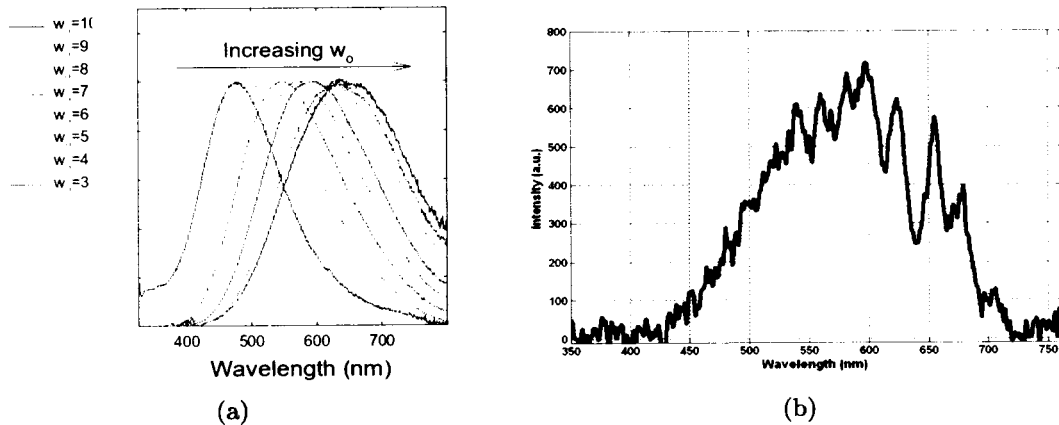


Figure II.6: (a): One-photon fluorescence spectrum specification of CdS particle sample with excitation wavelength around 300nm. The particle size w_0 is around 10nm. (b): Measured two-photon fluorescence spectrum of CdS particle sample with an excitation wavelength at 800nm. By comparing the one-photon and two-photon spectra, the result from the two-photon fluorescence microscope platform is reasonable.

Raster Scanning

To test the raster scanning capability of the system, an SU8 structure fabricated on a silicon substrate is examined with this system. Normally photo-resist materials have a large two photon cross section. The microscope image is shown in figure II.7, and not many details can be observed. The two-photon fluorescence scanning image is shown in figure II.8 with a line scan in the inset. It's much clearer and more details are revealed.

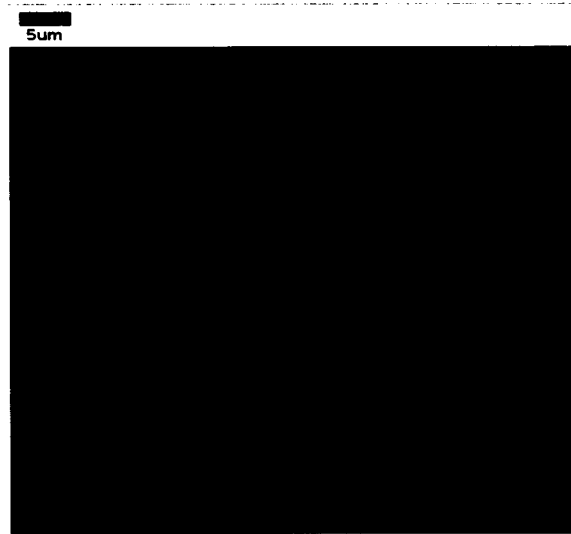


Figure II.7: Optical image of SU8 structure on a silicon substrate. The image is blurry and not many details can be observed.

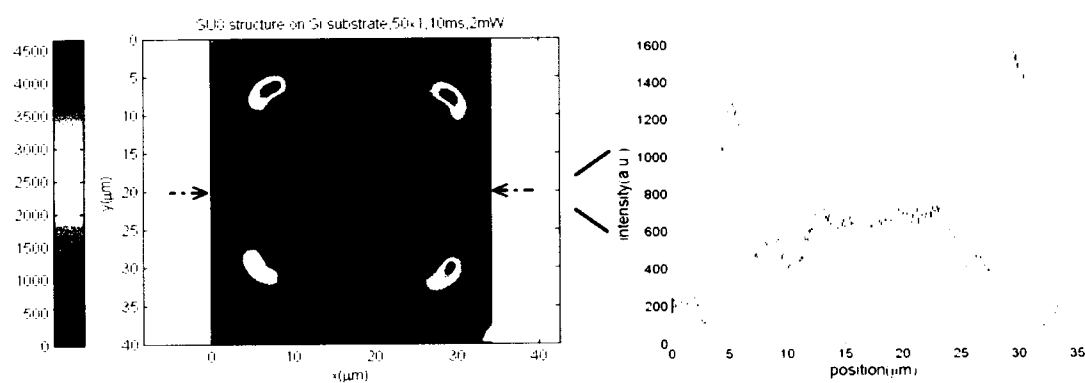


Figure II.8: Two photon fluorescence scanning image of SU8 structure on silicon substrate. A line scan is shown in the inset. More details are revealed. The image resolution is 95.25nm.

CHAPTER III

TWO-PHOTON FLUORESCENCE IMAGING OF RUTHENIUM METAL COMPLEX IN LIVING A431 CELLS

Background

The purpose of this project is to probe Titanium dioxide (TiO_2) nano particles with Ruthenium (Ru) metal complex attached inside living A431 cells by detecting the two-photon fluorescence of Ru metal complex. With this capability, the activities invoked by Ru metal complex inside a living cell can be traced, which is a useful tool to reveal *in-vivo* cell activities. Possible application of the Ru metal complex includes probing specific cell signaling pathways and measuring intra-cellular redox potential.

Nano Particles Preparation

The nano particles are provided by the Chemical and Biological Sensors Group of University of Dayton Research Institute. The Ru metal complex is attached to TiO_2 nano particles through Dopamine, and the particle size is between 30nm and 50nm. The composite of a complete TiO_2 particle is shown in figure III.1. The particles are then dispersed in phosphate buffered saline (PBS) buffer with an appropriate concentration and added to cell medium.

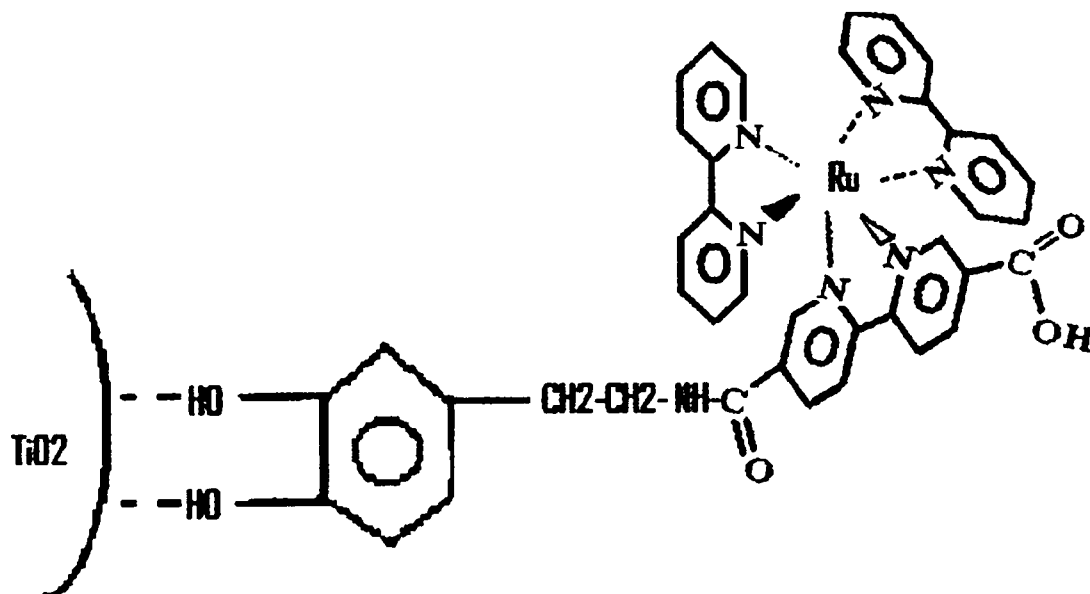


Figure III.1: The chemical composite of TiO_2 nano particles with Ru metal complex attached through dopamine.

System Optimization

In order to maintain the cell's viability, only the oscillator is used as the laser source, and the power is turned down as low as possible while maintaining a signal.

The two-photon fluorescence intensity of pure Ru metal complex with respect to the input power and the fitting curve are shown in figure III.2. A quadratic relation is clearly identified, which is a signature of a two-photon process. The two-photon fluorescence spectrum of Ru complex is given in figure III.3.

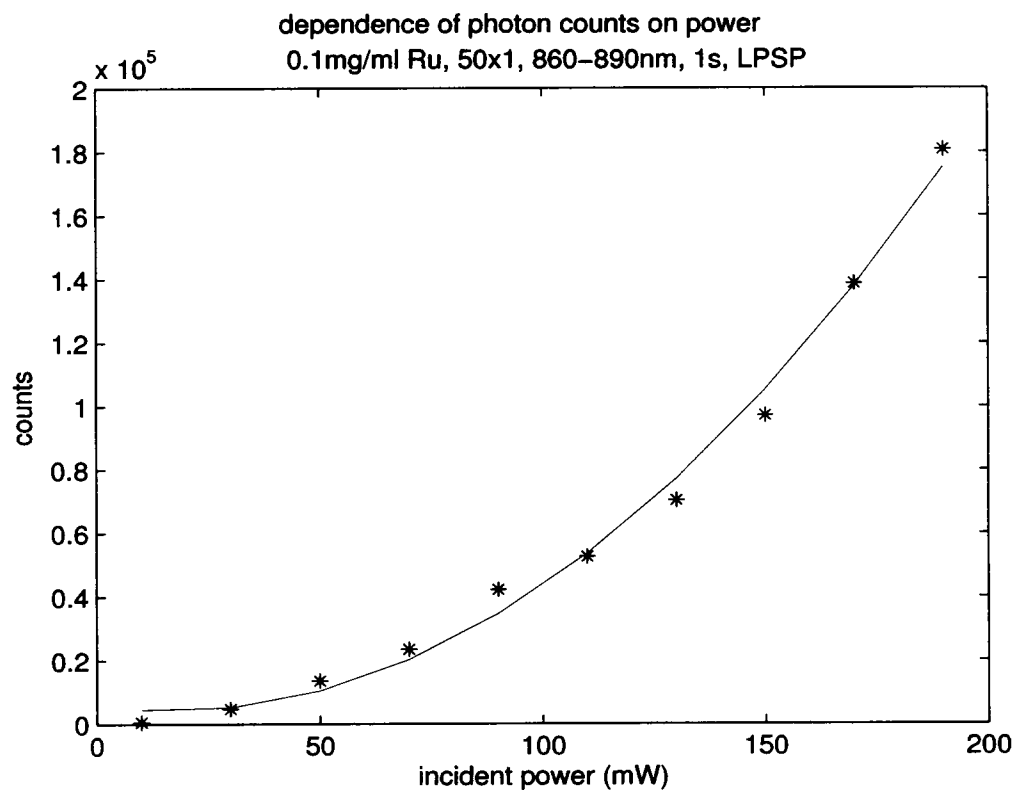


Figure III.2: Two-photon fluorescence intensity versus input laser power of Ru metal complex. The solid line is a fitted quadratic curve. A quadratic relation is clearly identified.

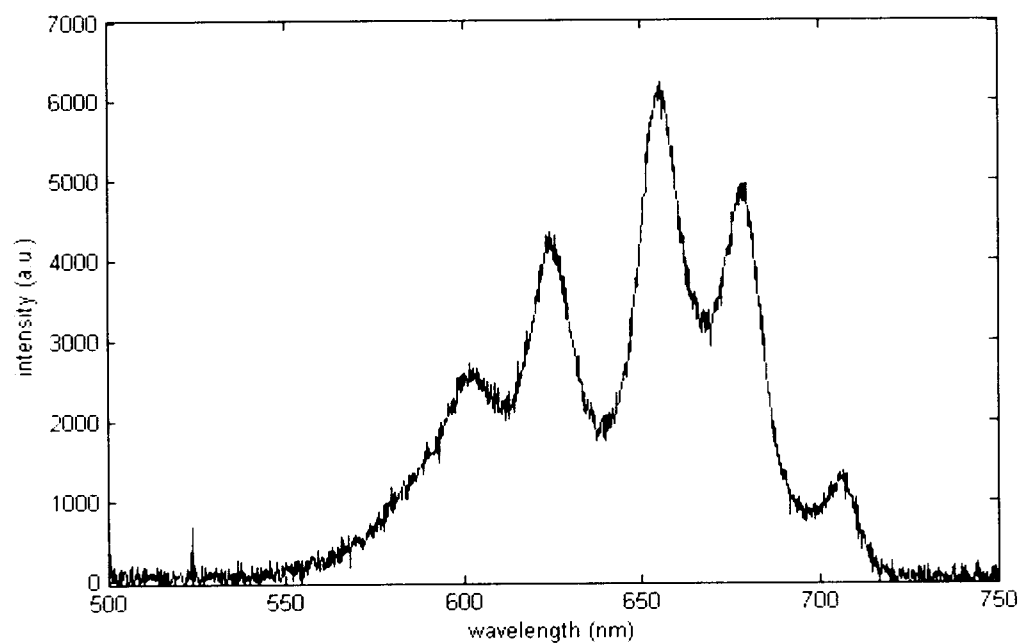
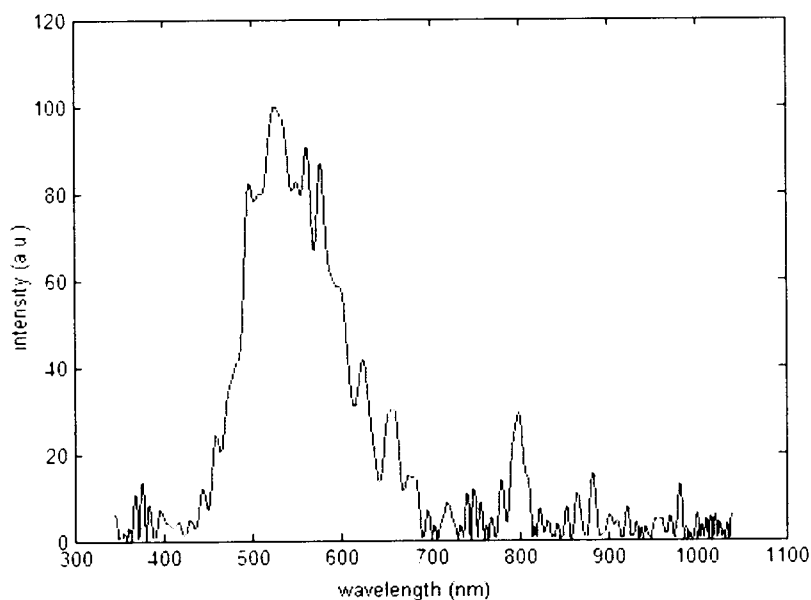


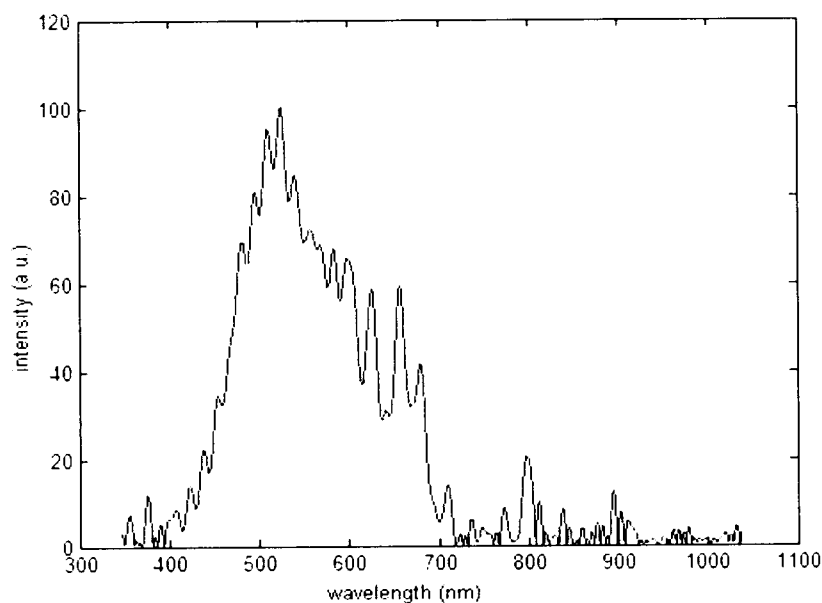
Figure III.3: Two-photon fluorescence spectrum of Ru metal complex. The objective in use is 50x1.5. Excitation wavelength is centered at 800nm. Then the fluorescence signal from Ru metal complex is mainly between 600nm and 700nm.

The fluorescence signal of the Ru metal complex will be used to determine the position of the nano-particles. There are two main reasons for this. First, it is not guaranteed that Ru complex is attached to every TiO_2 particle, so tracing the Ru complex directly is more accurate. Second, the two-photon fluorescence of the TiO_2 particle is within 400nm and 600nm, which is also within the fluorescence spectra of the cells and cell medium. There is much less background noise within the band of fluorescence signals from the Ru metal complex (600~700nm). Therefore, a band-pass filter needs to be selected carefully to collect only the two-photon fluorescence signal of the Ru metal complex.

Based on the comparison of the fluorescence spectra of ' TiO_2 +Dopamine' particles in figure III.4(a) and that of ' TiO_2 +Dopamine+Ru' particles in figure III.4(b), a band-pass filter with window 568.2nm to 785nm is chosen to collect the emission light. It is composed of a 785nm short pass RazorEdge filter (Semrock, NY) and a 568.2nm RazorEdge Long Wave Pass filter (Semrock, NY).



(a)



(b)

Figure III.4: Processed two-photon fluorescence spectra of TiO_2 particles. (a): TiO_2 particles only with Dopamine. (b): TiO_2 particles with Ru complex attached through Dopamine. The objective in use is 50x1.5. Excited wavelength is centered at 800nm. There is an obvious difference between 600nm and 700nm.

By looking at figure III.5, the emission signal with excitation wavelength between 860nm and 890nm has the highest Ru fluorescence and relatively low 'TiO₂+Dopamine' fluorescence signal. So excitation wavelength region can be chosen to be 860nm-890nm.

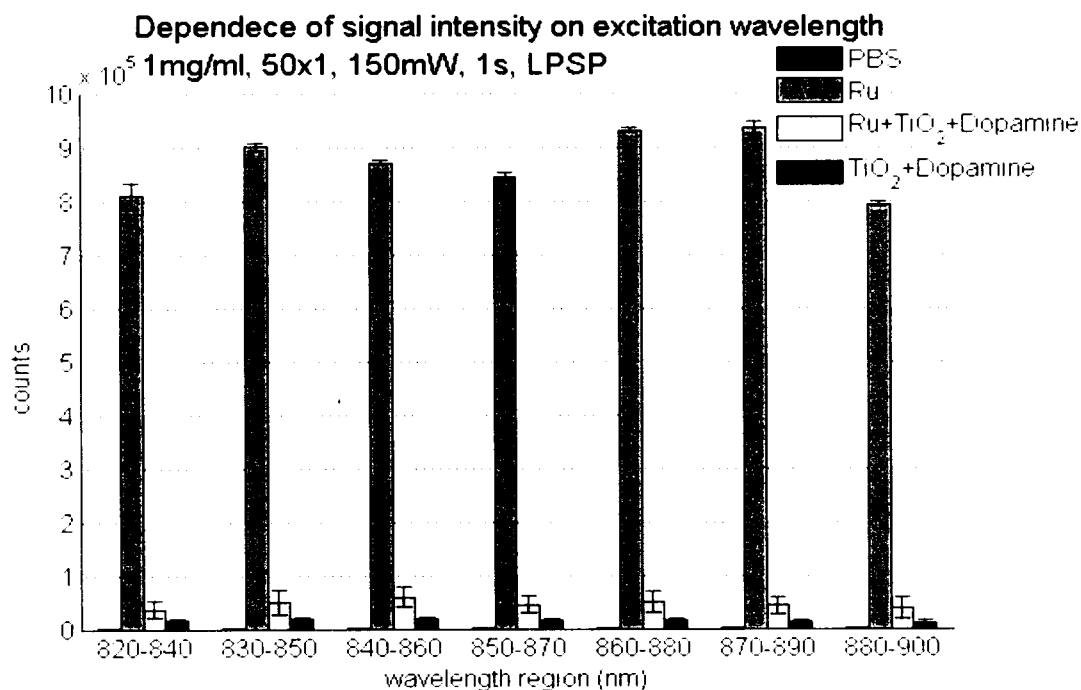


Figure III.5: Bar graph showing fluorescence intensity under different excitation wavelength for Ru complex and particles. The emission signal with excitation wavelength between 860nm and 890nm has the highest Ru fluorescence and relatively low 'TiO₂+Dopamine' fluorescence signal.

A431 Cell Preparation

A431 cells are provided by the Prof. Tsonis group from Biology Department at the University of Dayton. For preparation, cells are exposed to $1\mu\text{g}/\text{ml}$ particle solutions for more than 12 hours. Over this period of time, the nano particles will enter the cells. For comparison, a dish of ordinary cells is also processed under exactly the same condition without adding nano particles as a control. Before they are brought to the platform, all cell dishes are washed by PBS to get rid of the particles outside cells.

Two-photon Fluorescence Imaging of A431 Cells

After all the preparations, the cells with and without nano particles inside are imaged using the two-photon system. Two scanning images of cells with particles inside are shown in figure III.6 and figure III.7. As a comparison, a scanning image of ordinary cells without exposure to nano particles is shown in figure III.8. From the fluorescence images, the cell boundaries can be clearly discerned. More contrast and distinctive dots can be observed on the scanning image of cells with particles. It is supposed to be related to the TiO_2 nano particles with Ru inside the cells.

However, many dots have a size around $0.5\mu\text{m}$, which is 10 times larger than the size of the nano particles. And some dots have very a high fluorescence signal. One possible explanation is that nano particles get aggregated during the process and there are some unknown signals. More studies are necessary to make a more definitive conclusion, such as independent verification of the nano particle size. Other issues are discussed in the summery chapter.

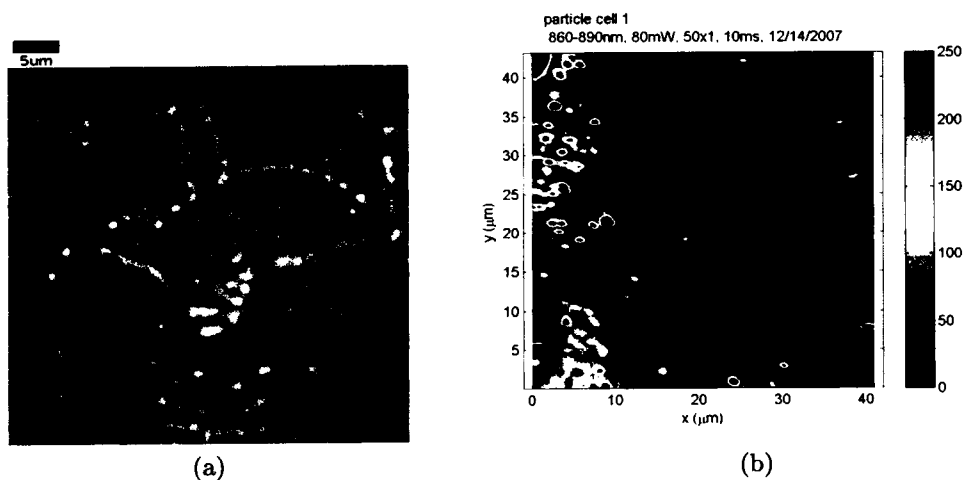


Figure III.6: A scanning image of cells with particles inside. (a): optical image of scanning area under microscope. (b): two-photon fluorescence image. The magnification is 50x with $NA=0.80$. Incident power is 80mW. The translation speed is $9.525\mu m/s$ and the pixel size is $0.09525\mu m$.

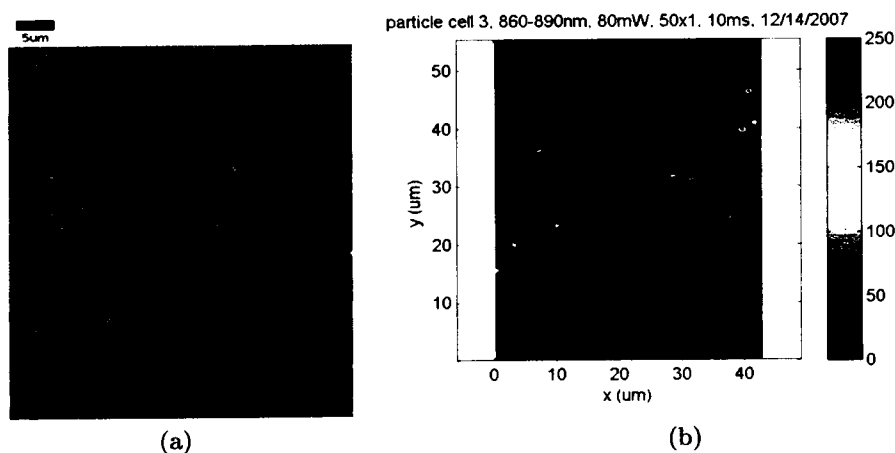


Figure III.7: Another scanning image of cells with particles inside. (a): optical image of scanning area under microscope. (b): two-photon fluorescence image. The magnification is 50x with $NA=0.80$. Incident power is 80mW. The translation speed is $9.525\mu m/s$ and the pixel size is $0.09525\mu m$.

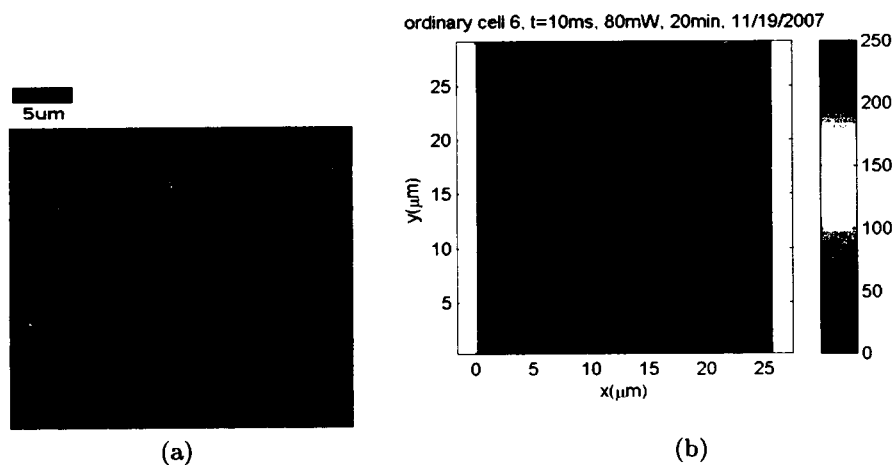


Figure III.8: A scanning image of ordinary cells as a comparison. (a): optical image of scanning area under microscope. (b): two-photon fluorescence image. The magnification is 50x with $\text{NA}=0.80$. Incident power is 80mW. The translation speed is $9.525\mu\text{m}/\text{s}$ and the pixel size is $0.09525\mu\text{m}$.

CHAPTER IV

LASER DIRECT WRITING INSIDE LiNbO_3

CRYSTAL

Background

Modification of materials with ultra-fast lasers[14] has recently attracted considerable interest because of its relevance to a wide range of applications including integrated optics[15], optical data storage[16], three-dimensional micro-[17] and nano-structuring[18]. Direct-writing technologies are of increasing importance in materials processing. In such an approach, structures are built directly without the use of masks, allowing rapid prototyping.

In particular, refractive index changes[19] and micro-explosion-induced voids[20] have been demonstrated in LiNbO_3 crystal, an important material for optical applications. It is a ferroelectric crystal that exhibits large birefringent, pyroelectric, piezoelectric, electro-optic, elastic, photoelastic, and bulk photovoltaic effects[21]. Fine optical or photonic structures inside LiNbO_3 can enhance nonlinear processes such as quasi phase matching and harmonic generation.

To make use of the structural modifications that are patterned inside nonlinear crystal, their basic characteristics need to be investigated. The index of refraction is an important characteristic. Because the structural modification is transparent

and its index change is expected to be small, the phase information can be useful to determine the index of refraction. In this thesis, quantitative phase microscopy (QPM)[22] is employed to obtain quantitative phase data from microscopic phase samples, and the index change can be calculated from the phase data.

Consider a perfect, aberration-free optical microscope of high numerical aperture and a coherently illuminated object with both phase and amplitude structure. The field leaving the object can be described by the complex function

$$O(x, y) = A(x, y) \exp[i\phi(x, y)] \quad (\text{IV.1})$$

where, in the case of a two-dimensional object, $A(x, y)$ represents the object's absorption profile and $\phi(x, y)$ is its phase profile. The field goes through the microscope system and at the image plane the intensity distribution is given by

$$I_{\text{image}}(x, y) = |A(x/M, y/M)|^2 I_{\text{illum}}(x, y) \quad (\text{IV.2})$$

where $I_{\text{illum}}(x, y)$ is the intensity distribution in the absence of the object and M is the image magnification.

Suppose the intensity in the image space is $I(x, y, z)$ and focal plane is at $z = 0$. Then the intensity at the image plane is $I(x, y, 0)$. The introduction of a small amount of defocus near the image plane is mathematically equivalent to a differential propagation of the field and can be described by the so-called transport of intensity equation (TIE)[23]:

$$k \frac{\partial I(x, y, z)}{\partial z} = -\nabla_{\perp} \cdot [I(x, y, z) \nabla_{\perp} \phi(x, y, z)] \quad (\text{IV.3})$$

where $k = 2\pi/\lambda$. Assume the illumination is coherent, meaning $I_{Illum}(\mathbf{r})$ is a constant. The transparent sample has mainly phase changes, so the intensity change at the focal plane is negligible. Then $I(x, y, 0)$ can also be treated as a constant with a notation of I_0 . At the focal plane, equation IV.3 can be rewritten as

$$k \left. \frac{\partial I(x, y, z)}{\partial z} \right|_{z=0} = -I_0 \nabla_{\perp}^2 \phi(x, y, 0) \quad (\text{IV.4})$$

Applying Fourier-transform methods,

$$\phi(x, y, 0) = \frac{k}{I_0} \cdot \mathcal{F}_{2D}^{-1} \left[\frac{\mathcal{F}_{2D}(I'_z|_{z=0})}{q^2} \right] \quad (\text{IV.5})$$

where the subscript $_{2D}$ means 2-dimensional Fourier transform and q means the Fourier transform variable.

In order to obtain a quantitative phase image, one collects an in-focus image and very slightly positively and negatively defocused images. They can be used to estimate the differential with respect to the defocus of the image. Once the phase map is obtained by equation IV.5, the refractive index change can be easily calculated using the relationship:

$$\Delta n(x, y) = \frac{\lambda \Delta \phi(x, y)}{2\pi t} \quad (\text{IV.6})$$

where λ is the wavelength at which the phase is measured and t is the thickness of the slice.

To demonstrate the procedure, a fiber is examined with this algorithm. It is a 630HP single mode fiber (Thorlabs, NJ) immersed in a type of immersion oil (FRYER, IL) with index around 1.5. The immersion oil is used to match the index refraction of the cladding, so that the phase changes are mainly due to the difference

between the refractive index of the cladding and core. A 532nm laser line filter (Semrock, NY) with a bandwidth of 3nm is used in the optical path. The in focus image of the fiber is shown in figure IV.1(a). Then two images defocused by $\pm 2\mu m$ are taken to calculate the phase shift across the core of the fiber. The defocused images are shown in figure IV.1(b) and figure IV.1(c).

Using the QPM algorithm, the calculated phase profile around the core area is in figure IV.2(a) and a line scan in figure IV.2(b).

From the line scan, the phase shift across the fiber core is

$$\Delta\phi = 0.2 \text{ radians}$$

The thickness of the core is $t = 4\mu m$. Because of the connection between the phase difference and index difference

$$\Delta n = \frac{\lambda \Delta\phi}{2\pi t}$$

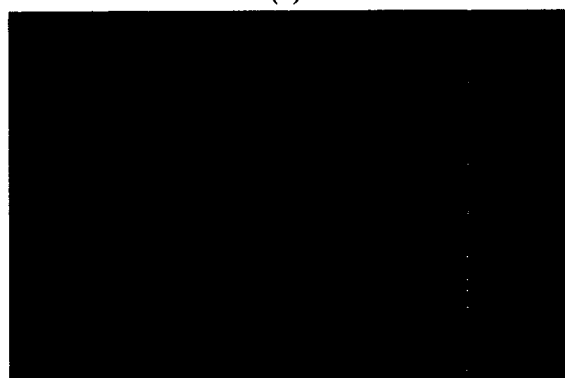
With $\lambda = 532nm$, the index difference is

$$\Delta n = 0.004$$

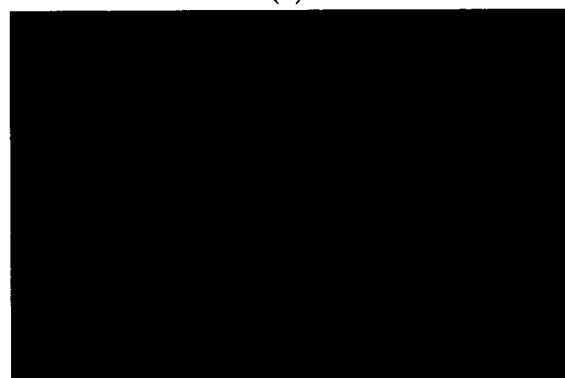
The index result correctly identify a positive index change and the value is reasonable. This proves the correctness of the algorithm.



(a)

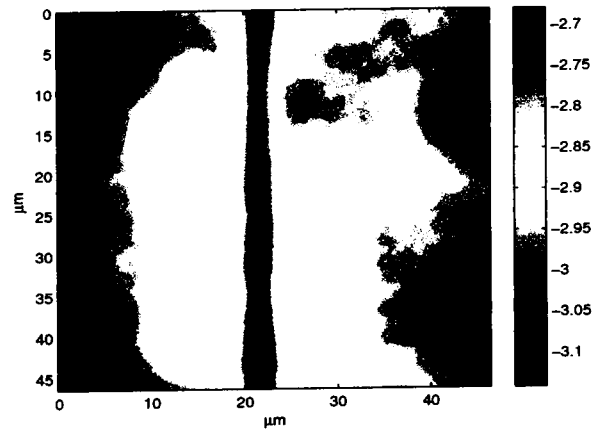


(b)

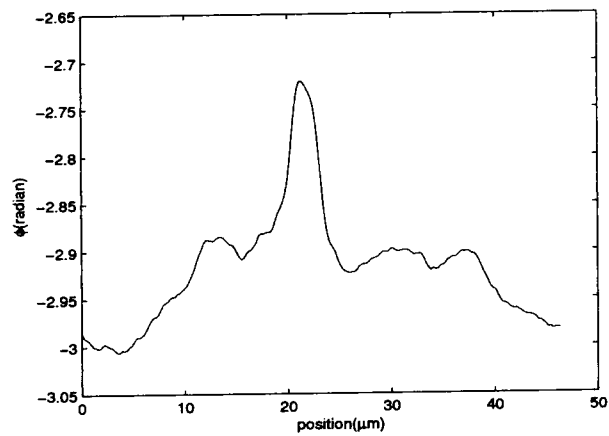


(c)

Figure IV.1: Optical image of oil-immersed 630HP fiber under microscope after a 532nm laser line filter. (a): fiber in focus. (b): fiber defocused at $+2\mu m$. (c): fiber defocused at $-2\mu m$. The magnification is 20x1 and numerical aperture is 0.50.



(a)



(b)

Figure IV.2: Calculated phase profile of 630HP single mode fiber around the core area. (a): 2D phase map (b): line scan. The phase shift between core and cladding is about 0.2 radians.

System Optimization

High pulse energy is necessary for directly writing patterns inside LiNbO_3 , so the amplifier is used as the laser source. The basic scheme is shown in figure IV.3. There is no need to collect any signal. The quarter wave plate is not necessary either since the amplifier is much more stable. The linear polarizer is kept in the optical path to adjust the total power level. The focusing beam is linearly polarized.

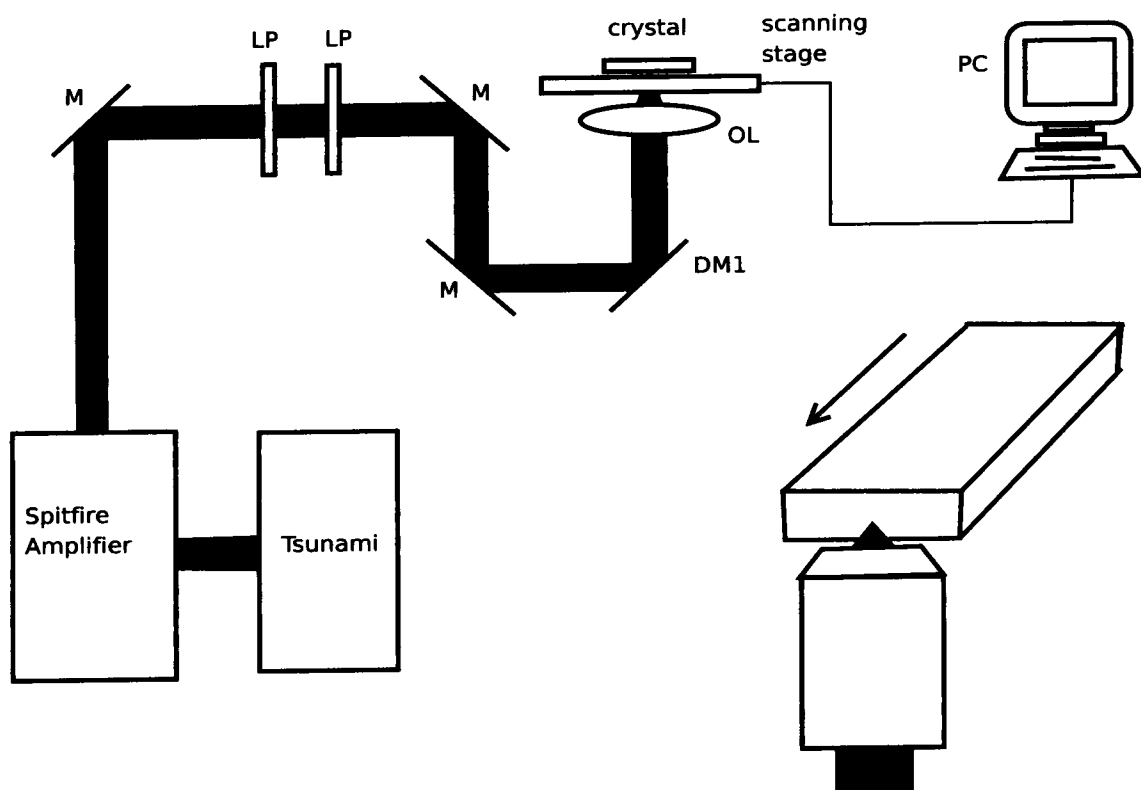


Figure IV.3: A scheme of the laser direct writing inside crystal setup. M: mirror; LP: linear polarizer; OL: objective lens; DM: dichroic mirror.

Structural Modification

When line patterns are being written inside the crystal, if the power is high enough, small explosions will occur at the focus, causing some damage in the focal area. By carefully controlling the power level, transparent structural modification can be written inside the crystal. Moreover, controlling power level and the objective can change the profiles of depth of focus (DOF). If the numerical aperture (NA) is low, an elliptical DOF is expected. If NA is high enough, a round DOF is possible. Some elliptical DOF profiles are shown in figure IV.4, while some round DOF profiles are in figure IV.5. So the system is able to write lines with different DOF profiles.

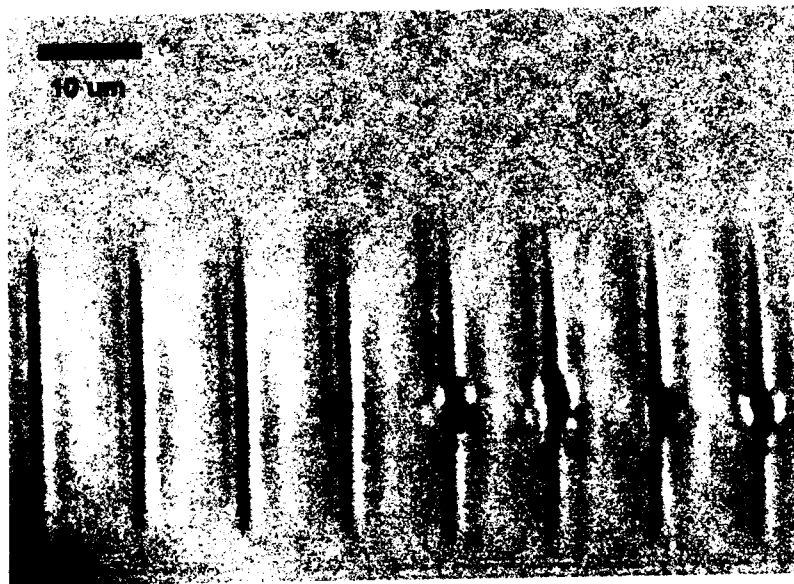


Figure IV.4: Elliptical DOF profiles of line patterns inside LiNbO_3 crystal, which have a width of $2 \sim 4 \mu\text{m}$ and a height of $10 \sim 20 \mu\text{m}$. These patterns are written 200 μm inside the crystal with 20x1.5 magnification and $\text{NA}=0.5$. The left four DOF profiles are written with power of 40mW and the other four DOF profiles are with power 50mW. The velocity of the stage is $100 \mu\text{m/s}$. Under this condition, the breaking threshold power is between 40mW and 50mW.

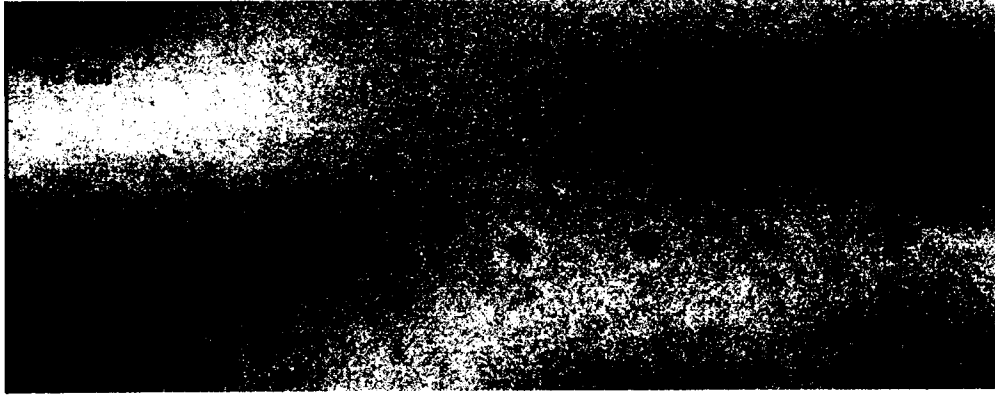


Figure IV.5: Round DOF profiles of line patterns inside LiNbO₃ crystal, which has a diameter of only $1 \sim 2\mu m$. These patterns are written 50 μm inside the crystal with 50x1.5 magnification and NA=0.80. The laser power is only 0.45mW. The velocity of the stage is 100 $\mu m/s$. The image is contrast-enhanced for better display.

Measuring Index Change of Structural Modification

To measure the index change of the structural modification inside LiNbO₃, some line patterns are written 70 μm beneath the surface. The DOF profiles are captured in figure IV.6. Two defocused images of one line pattern with a distance of 8 μm in z direction are shown in figure IV.7. These two images are contrast enhanced for better display. The filter in use to capture these defocused images has a passing band of $650 \pm 20nm$ (Thorlabs, NJ).

After applying the QPM algorithm on these images, the calculated phase map of the pattern area is shown in figure IV.8. A line scan is shown in figure IV.9.

According to the calculated phase profile, the phase shift around the pattern is

$$\Delta\phi = -0.04 \text{ radians}$$

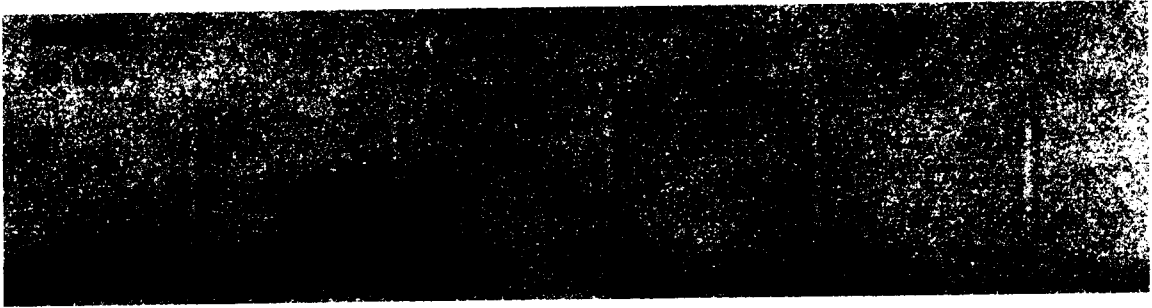


Figure IV.6: The DOF profiles of line patterns inside LiNbO₃ crystal. The patterns are 70 μ m under surface. The magnification is 20x1. Translation speed of the stage is 50 μ m/s. Incident laser source is 5kHz femtosecond laser from the amplifier with average power of 3.00mW. The height of these patterns is around 10 μ m.

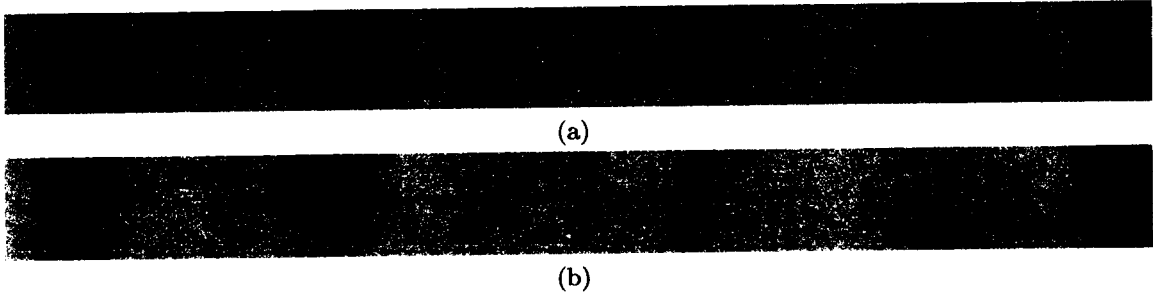


Figure IV.7: Two defocused optical images of one line pattern inside LiNbO₃ crystal after white light transmission illumination from microscope and a 650 ± 20 nm band-pass filter. (a) pattern at position 0 μ m. (b): pattern at position +8 μ m. The image is contrast enhanced for display purpose.

With $\lambda = 650$ nm, $t = 10\mu$ m, the index difference between the structural modification and pure crystal is

$$\Delta n = \frac{\lambda \Delta \phi}{2\pi t} = -4 \times 10^{-4}$$

It needs to be pointed out that the index of the structural modification is smaller than the pure crystal, which is useful in the future photonics structure design.

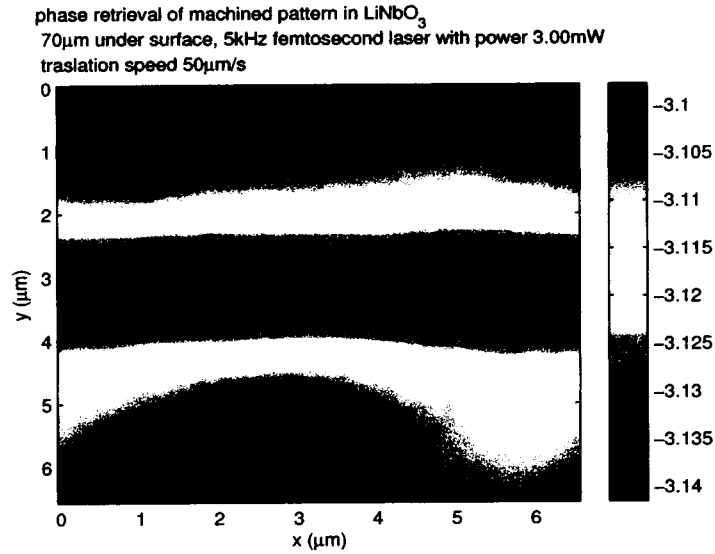


Figure IV.8: The calculated phase map of a line pattern inside LiNbO_3 crystal. The unit of the colorbar is *radian*.

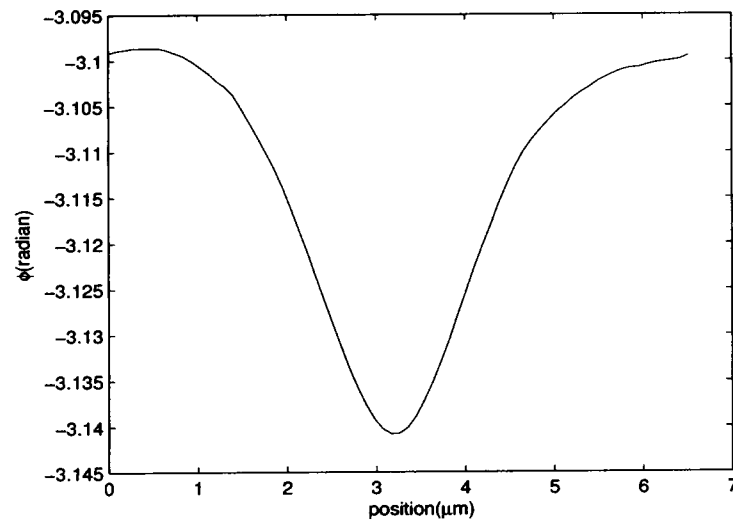


Figure IV.9: A line scan of the calculated phase map of a line pattern inside LiNbO_3 crystal. The index difference between the structural modification and the pure crystal is -0.04radians

CHAPTER V

SUMMARY AND DISCUSSIONS

In this thesis, a scanning microscope platform has been built and the instrumentation is described in detail. Two research projects have been operated on this platform.

The first one is two-photon fluorescence imaging of TiO_2 nano particles with Ru metal complex attached inside living A431 cells. In preparation, A431 cells are exposed to TiO_2 nano particles with Ru metal complex attached through Dopamine so that the nano particles will go through cell membranes. Then the cells are inspected under the microscope platform and two-photon fluorescence cell images are generated to probe nano particles with Ru attached inside the living cell. By comparing the fluorescence images of cells with nano particles inside and those without, the spatial distribution of TiO_2 nano particles with Ru attached can be detected.

Right now this project needs further improvement. The fluorescence signal from the Ru metal complex is very weak and is easily affected by fluorescence emissions of cells and cell medium. There are some reasons for that. First of all, the nano particles are diluted to a very low concentration ($< 1\mu\text{g/ml}$) and it is not guaranteed that all of them can pass the membrane. Secondly, the two-photon cross section of the Ru metal complex is not as high as that of dyes. The result of these is that higher pulse energy is needed to get enough fluorescence signals from Ru metal complex. Higher pulse energy also brings more background noise. In the future, better chemical and biological processing can be developed to increase the nano particle concentration

inside cells. On the other hand, other composites or nano particles (such as gold nano rods) with larger two-photon cross sections can be chosen for possible applications.

The second project is laser direct writing inside LiNbO_3 with tightly focused femtosecond laser. Line patterns with width of several microns can be directly written inside the crystal. The depth of focus can be controlled to have either an elliptical shape with a height of $10 \sim 20 \mu\text{m}$ or a round shape with a diameter of only $1 \sim 2 \mu\text{m}$ if incident pulse energy and objective lens are carefully chosen. Two defocused optical images are taken to compute the phase profile around the structural modification area using a quantitative phase microscopy algorithm. The index change calculated from the phase profile is -4×10^{-4} . This is a useful characteristic of the structural modification in the crystal. With definitive index change data available, optical structures can be designed and written inside the crystal to enhance nonlinear processes in LiNbO_3 crystals.

However, it has been proposed recently[24] that laser writing in LiNbO_3 can be seen as a new non-reciprocal, nonlinear optical phenomenon. When the direction of the femtosecond laser beam is reversed from the $+z$ to $-z$ direction, the structures written in LiNbO_3 crystal when translating the beam along the $+y$ and $-y$ directions are mirrored. And different sign of index change has been observed under different pulse energy and translation direction in the y axis. It is necessary to look into this issue in the future and investigate the index change thoroughly. Meanwhile, the system needs to be optimized to get better optical images and the algorithm can be improved to include image processing and iteration.

The two-photon fluorescence project uses circular polarization and current direct writing project uses linear polarization. Both are typical spatially homogeneous polar-

ization states. Beams with spatially inhomogeneous polarization, such as cylindrical-vector beams[25], have some unique focusing properties and a very strong axial field component. A tighter focal spot can be achieved using radially polarized light focused by a high numerical aperture (NA) objective lens [26]. The strong axial field component may be used to enhance some nonlinear process, such as THG[27].

More generally, a spatial light modulator (SLM) is able to generate arbitrary wavefronts. With some polarization elements, arbitrary polarization on every pixel is feasible. Thus the incident laser beam can be engineered to achieve tighter focal area or optimized depth of focus.

APPENDIX A

USER MANUAL FOR LABVIEW MASTER PROGRAM

This is the manual for the labview master program **Blended Vector Move v5** which is responsible for device parameters setup, device synchronizations, raster scanning control and data collections for the scanning microscope platform. This version fetches signal data from the photon counter (SRS, CA) through a GPIB interface. Other versions of this master program get data from other devices like oscilloscope or data acquisition card. After all, it is easy to modify the master program to adapt to different devices.

The computer that hosts the Labview master program needs to communicate with the XY microstage (Mad City Labs, WI) and the SR400 gated photon counter (SRS, CA). The microstage is connected to the computer through a National Instruments 73xx Motion Controller PCI card, and the SR400 photon counter communicates with the computer through GPIB port. The computer should have Labview main program and NI-Motion driver software installed. The recommended Labview version is 8.2. When installing NI-Motion, please include all options for easy using.

The master program has a dependence on the Mad City Labs Nanopositioning labview drivers (comes with the microstage), SR400 gated photon counter labview drivers (can be downloaded from Internet) and some supplementary VIs. It can only

function correctly with the XY micro-stage driver and photon counter connected and powered on.

When the Labview master program is turned on, it is running an infinite loop and waiting for commands. It is built on an event-based model. The front panel is shown in figure A.1. It is divided into several sections, which are “NI-Motion Parameters”, “Move Around”, “Control Center”, “INPUT”, “Nano Stage Output”, “counter parameters” and “Scope Output”. Operations and functions of every section will be explained in detail in the rest part of the manual.

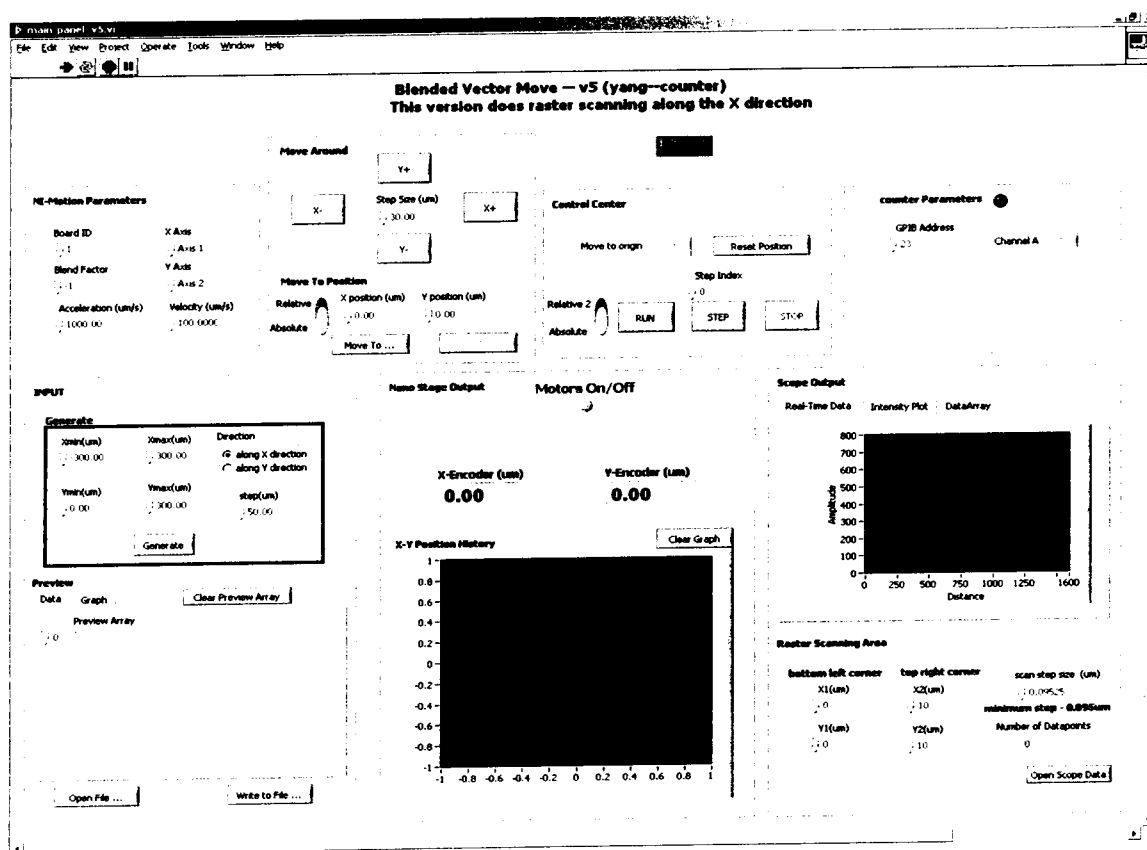


Figure A.1: A screenshot of first running front panel of Labview master program.

NI-Motion Parameters

NI-Motion Parameters	
Board ID	X Axis
1	Axis 1
Blend Factor	Y Axis
-1	Axis 2
Acceleration (um/s)	Velocity (um/s)
1000.00	100.0000

The 'NI-Motion Parameters' is in the upper left corner. It defines basic parameters for the NI 73xx Motion Controller PCI Card and the MCL microstage. The 'Board ID' is 1; 'Blend Factor' is -1; 'X Axis' is Axis 1; 'Y Axis' is Axis 2. These four options are default values and there is no need to change them. The other two parameters are 'Acceleration($\mu\text{m}/\text{s}^2$)' and 'Velocity($\mu\text{m}/\text{s}$)', whose meanings are very straightforward. They can be set to appropriate values according to specific needs.

It is worth to emphasize here that the microstage is in stepping mode and the minimum step size is 95.25nm . If the velocity is $0.09525\mu\text{m}/\text{s}$, the stage will execute a step once and then wait until 1 second elapses.

Move Around

The screenshot shows a control interface for moving a stage. It is divided into two main sections: 'Move Around' and 'Move To Position'.

Move Around Section:

- Four directional buttons: X-, X+, Y-, and Y+.
- A 'Step Size (um)' input field with a value of 30.00.

Move To Position Section:

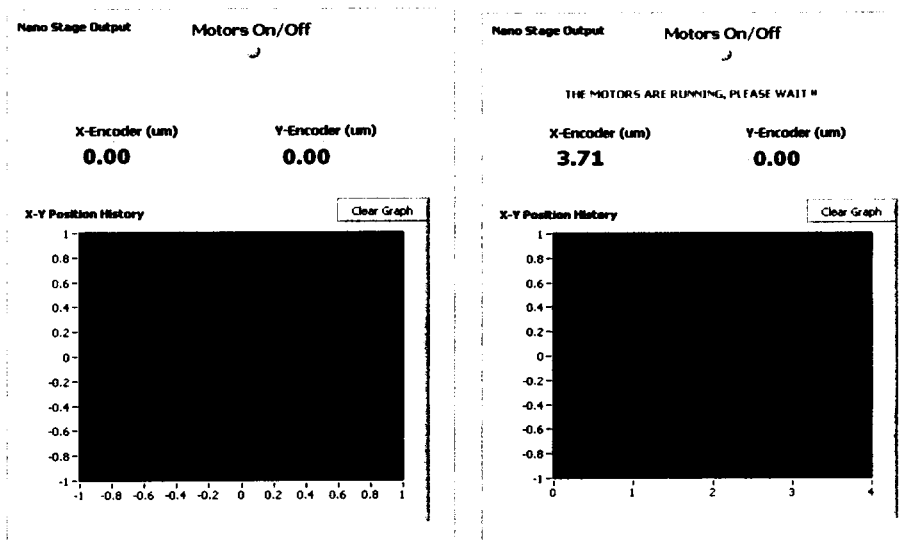
- Two radio buttons: 'Relative' (selected) and 'Absolute'.
- Two input fields for 'X position (um)' and 'Y position (um)', both showing 0.00.
- A 'Move To ...' button.

The 'Move Around' section is very handy when moving the stage around. Once a direction button is pressed, the stage will move a distance of the defined 'step size' relative to current position toward that direction. The minimum step size is 95.25nm. These four direction buttons are mapped to the four keys, Home, End, Delete and Page Down for more convenience. The key mappings can be changed as one likes.

It needs to be mentioned here that the actual stage moving directions may not be the same as those in your first thought. It is better to confirm the relation between the direction buttons and the actual moving directions through some simple tests.

The 'Move To Position' part allows an accurate coordinates of the destination, either in an absolute coordinate or a relative coordinate with respect to current position. By pressing the 'Move To ...' button, the stage will move the the destination point. The 'STOP MOVING' button can be used to interrupt the moving process.

Nano Stage Output



The 'Nano Stage Output' section refreshes the status of microstage automatically, providing both current coordinates and the coordinates history. When the stage is moving, a warning text will appear.

Input & Control Center

The 'INPUT' and 'Control Center' sections are closely related. The 'INPUT' section is used to design stage moving routes and 'Control Center' section controls the execution of the microstage path.

There are two ways to design microstage routes. The first is to use the 'Generate' function to generate simple raster scanning pattern. The detail is explained in figure A.2. This is an easy way to make simple zigzag scanning paths. After generation, the path will be shown in the 'Preview' part in both array and graph forms for correction and modification. Another way is to load path data from a text file. The file should only have 2 lines, one lines the x coordinates of all the points in sequence and the other line the y coordinates, separated by a tab letter. Below is a sample.

```
x1 x2 x3 x4 ...
y1 y2 y3 y4 ...
```

This path from this file will go through $(x_1, y_1) \Rightarrow (x_2, y_2) \Rightarrow (x_3, y_3) \Rightarrow \dots$. The current path can also be saved into text file by clicking the 'Write to File' button. With this ability, arbitrary moving routes can be designed.

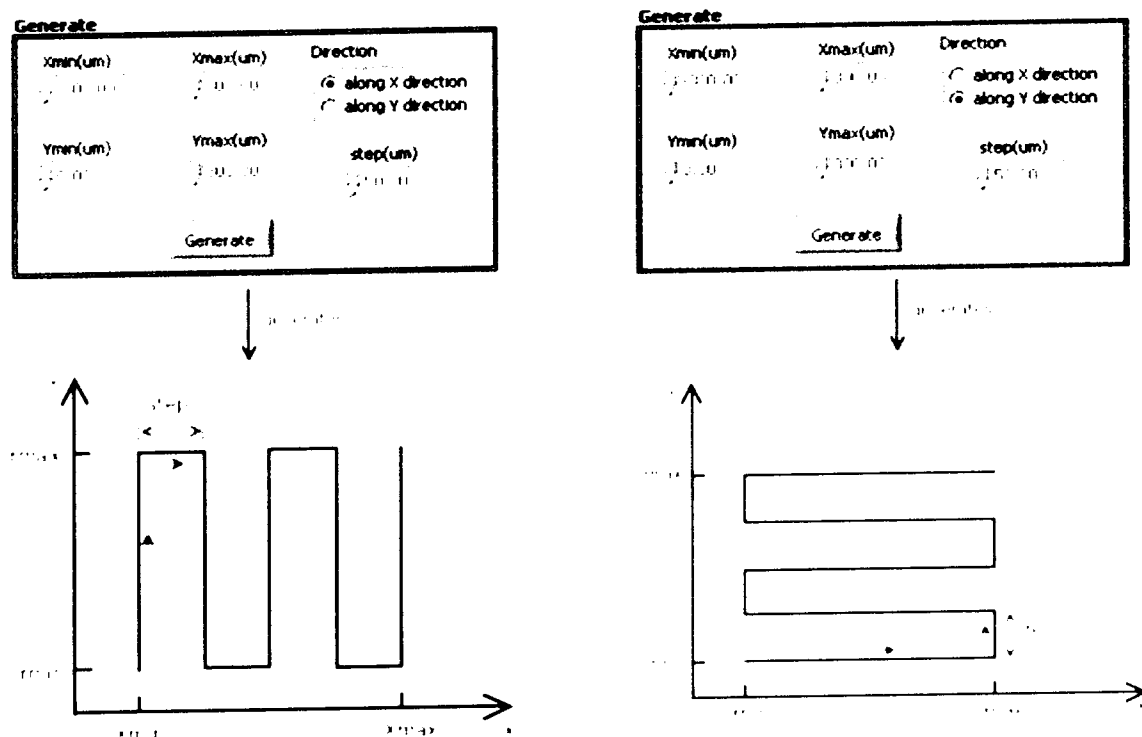


Figure A.2: Figure showing the stage route using 'Generate' function in the 'INPUT' section. The 'Direction' option gives a little flexibility.

When a path is ready, the 'Control Center' section is responsible for controlling the movement. When the 'RUN' button is pressed, the microstage will start moving following the path defined in the 'INPUT' section. The 'STOP' button can be used to bring stage to a halt. The 'STEP' button provides an ability to step down the path point by point, like the stepping in program debugging. The 'Step Index' shows the current point, and it can be changed to move to any index of points. The signature

in figure A.3 is made with this program by direct laser writing on LiNbO_3 surface with focused Ti:Sapphire mode-locking beam.

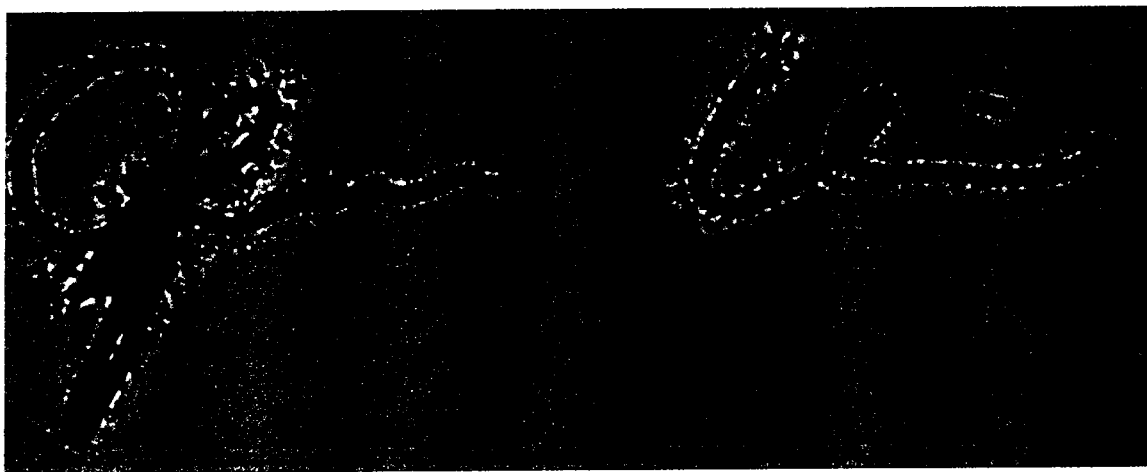
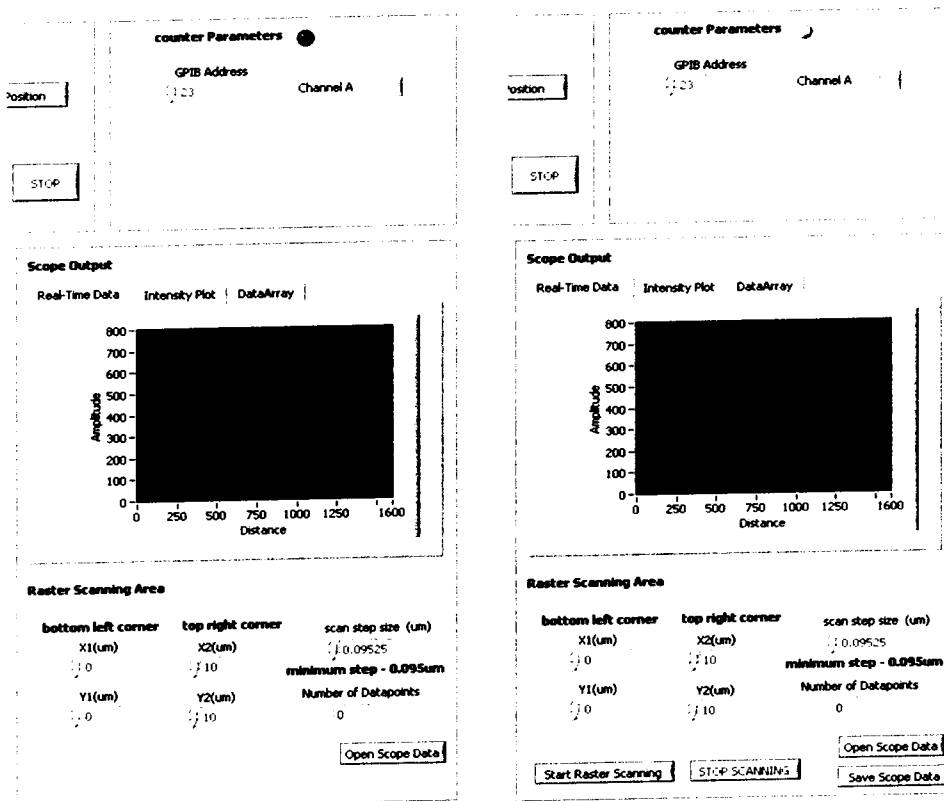


Figure A.3: A signature made with the labview master program on the surface of LiNbO_3 by direct laser writing with focused Ti:Sapphire mode-locking beam. This shows the ability of generating arbitrary patterns with the Labview master program.

There is a 'Reset Position' option in the 'Control Center' section. It can 'move the stage to the origin point' or 'reset current position as the origin point'. These are useful commands when choosing scanning areas.

Counter Parameters & Scope Output



The 'Counter Parameters' and 'Scope Output' sections communicate with both the microstage and the SR400 photon counter. It is mainly designed for high resolution nonlinear imaging. The photon counter collects enough response signals from sample while the stage is doing raster scanning, and then the signal data are processed to form an image of the scanning area. By default, these two sections are turned off, denoted by the dark green LED light near the caption. By clicking on the LED, they are turned on and the LED becomes light green, and several more buttons show up in the bottom of 'Scope Output' section, which is the key to start the raster scanning process.

The 'Counter Parameters' just set the interface and parameters of the SR400 photon counter. Although SR400 supports two channel, this version only uses 'Channel A'.

The 'Scope Output' section defines the scanning area and displays live data during the scanning. Before running the raster scan, it is crucial to set up right values for stage speed, SR400 photon counter parameters and scanning areas according to the scanning route. Otherwise, the scanning will not be successful. In this version, the raster scanning uses the zigzag scanning route illustrated in figure A.4. The photon counter is only working when the stage is moving from $X1$ toward $X2$ and it should have finished counting when the stage reaches $X2$, because at that time the Labview master program will begin to fetch signal data from the photon counter. That is to say, the working time of the photon counter must be less than the time for the stage to move from $X1$ to $X2$. The time needed for the stage to move from $X1$ to $X2$ is

$$\text{moving time} = (X2 - X1) / \text{moving velocity}$$

The total working time of the photon counter is defined as

$$\text{total working time} = \text{number of periods} \times (\text{counting period} + \text{dwell time})$$

where dwell time is usually set to 0 with the help of an external signal generator during the scanning.

During the scanning, the real time data for every line scan is shown in the tabbed region in the form of graph, intensity plot and raw data. After scanning finishes, the data array can be saved into text file in the format of 2D array.

Because the stage has a minimum step size of $95.25nm$, it is the maximum resolution along the y axis. To achieve the same pixel resolution along the x axis, the

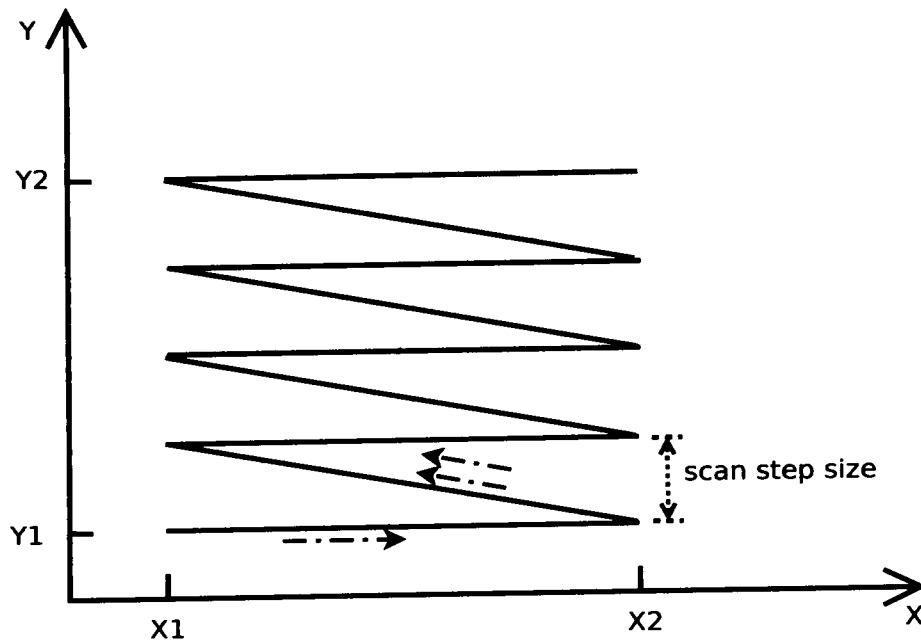


Figure A.4: The zigzag scanning route used in raster scanning with SR400 photon counter. The minimum scan step size is $0.09525\mu m$. When the stage begins to move from $X1$ to $X2$, the photon counter is triggered and starts collecting signals. When the stage reaches $X2$, the photon counter should have finished counting photons. Then the signal data are transferred through GPIB interface and stored in an array. The photon counter is stopped when the stage is moving back to $X1$ with a higher velocity. After that, a new loop starts until $Y2$ is reached along the Y axis.

stage velocity and the counting period of the photon counter needs to be configured as follows.

$$\text{resolution along } x \text{ axis} = \text{stage velocity} \times \text{counting period}$$

A configuration example is given here.

1. Use a separate Labview program to configure the SR400 photon counter. Use the internal 10MHz trigger signal. Set the 'T SET' counting period as 10ms, which is $1E5$ counts. Let the number of counting periods to be 500 (the maxi-

mum is 2000). The 'dwell time' is set to 0 and a 1MHz digital pulse generator is served as an external trigger to the photon counter (refer to the manual). So the actual dwell time is only $1\mu s$, which is negligible comparing to the counting period. Channel A is enables and its gate mode is set to 'CW', which means it will count all the signals within the counting period. The Determination Level is set to 100mV since the input is TTL pulses from an APD.

2. In the Labview master program, set the stage velocity as $9.525\mu m/s$. Then the x dimension of the scanning area should satisfy

$$\begin{aligned} |X_2 - X_1|_{min} &= \text{velocity} \times \text{counting period} \times \text{number of periods} \\ &= 9.525\mu m/s \times 10ms \times 500 \\ &= 47.625\mu m \end{aligned}$$

The y direction can be arbitrary. To speed up the whole scanning process, a higher stage velocity and shorter counting period can be used, with the number of periods and scanning area dimensions carefully chosen. Also the scanning area can be set at first, then appropriate number of counting periods and other parameters can be chosen accordingly.

Summary

This Labview master program provides a thorough control over the microstage and the photon counter. It is designed specifically for the scanning microscope platform. The block diagram of this Labview master program is open to all users and more versions can be derived from it. Thanks to Labview, it is easy to control devices through a simple interface without much programming and debugging effort.

BIBLIOGRAPHY

- [1] S. W. Hell. Far-field optical nanoscopy. *Science (New York, N.Y.)*, 316(5828):1153–1158, May 25 2007.
- [2] W. R. Zipfel, R. M. Williams, and W. W. Webb. Nonlinear magic: multiphoton microscopy in the biosciences. *Nature Biotechnology*, 21(11):1369–1377, Nov 2003.
- [3] L. Moreaux, O. Sandre, M. Blanchard-Desce, and J. Mertz. Membrane imaging by simultaneous second-harmonic generation and two-photon microscopy: errata. *Optics Letters*, 25(9):678, May 1 2000.
- [4] Y. Barad, H. Eisenberg, M. Horowitz, and Y. Silberberg. Nonlinear scanning laser microscopy by third harmonic generation. *Applied Physics Letters*, 70(8):922–924, FEB 24 1997.
- [5] M. C. Lang, J. Engelhardt, and S. W. Hell. 4pi microscopy with linear fluorescence excitation. *Optics Letters*, 32(3):259–261, Feb 1 2007.
- [6] J. X. Cheng, Y. K. Jia, G. Zheng, and X. S. Xie. Laser-scanning coherent anti-stokes raman scattering microscopy and applications to cell biology. *Biophysical Journal*, 83(1):502–509, Jul 2002.

- [7] B. Harke, J. Keller, C. K. Ullal, V. Westphal, A. Schonle, and S. W. Hell. Resolution scaling in sted microscopy. *Optics Express*, 16(6):4154–4162, Mar 17 2008.
- [8] Eric Betzig, George H. Patterson, Rachid Sougrat, O. Wolf Lindwasser, Scott Olenych, Juan S. Bonifacino, Michael W. Davidson, Jennifer Lippincott-Schwartz, and Harald F. Hess. Imaging intracellular fluorescent proteins at nanometer resolution. *Science*, 313(5793):1642–1645, SEP 15 2006.
- [9] Bo Huang, Wenqin Wang, Mark Bates, and Xiaowei Zhuang. Three-dimensional super-resolution imaging by stochastic optical reconstruction microscopy. *Science*, 319(5864):810–813, FEB 8 2008.
- [10] V. Kohli, A. Y. Elezzabi, and J. P. Acker. Cell nanosurgery using ultrashort (femtosecond) laser pulses: applications to membrane surgery and cell isolation. *Lasers in Surgery and Medicine*, 37(3):227–230, Sep 2005.
- [11] K. Schenke-Layland, I. Riemann, O. Damour, U. A. Stock, and K. Konig. Two-photon microscopes and in vivo multiphoton tomographs—powerful diagnostic tools for tissue engineering and drug delivery. *Advanced Drug Delivery Reviews*, 58(7):878–896, Sep 15 2006.
- [12] T. L. Spires, M. Meyer-Luehmann, E. A. Stern, P. J. McLean, J. Skoch, P. T. Nguyen, B. J. Bacskai, and B. T. Hyman. Dendritic spine abnormalities in amyloid precursor protein transgenic mice demonstrated by gene transfer and intravital multiphoton microscopy. *The Journal of Neuroscience : the official journal of the Society for Neuroscience*, 25(31):7278–7287, Aug 3 2005.

- [13] C. Xu and W. W. Webb. Measurement of two-photon excitation cross sections of molecular fluorophores with data from 690 to 1050 nm. *Journal of the Optical Society of America B-Optical Physics*, 13(3):481–491, MAR 1996.
- [14] A. C. Tien, S. Backus, H. Kapteyn, M. Murnane, and G. Mourou. Short-pulse laser damage in transparent materials as a function of pulse duration. *Physical Review Letters*, 82(19):3883–3886, MAY 10 1999.
- [15] J. W. Chan, T. R. Huser, S. H. Risbud, and D. M. Krol. Modification of the fused silica glass network associated with waveguide fabrication using femtosecond laser pulses. *Applied Physics A-Materials Science & Processing*, 76(3):367–372, MAR 2003.
- [16] K. Kawamura, M. Hirano, T. Kamiya, and H. Hosono. Holographic writing of volume-type microgratings in silica glass by a single chirped laser pulse. *Applied Physics Letters*, 81(6):1137–1139, AUG 5 2002.
- [17] S. Maruo and T. Saeki. Femtosecond laser direct writing of metallic microstructures by photoreduction of silver nitrate in a polymer matrix. *Optics Express*, 16(2):1174–1179, Jan 21 2008.
- [18] Y. Shimotsuma, P. G. Kazansky, J. R. Qiu, and K. Hirao. Self-organized nanogratings in glass irradiated by ultrashort light pulses. *Physical Review Letters*, 91(24):247405, DEC 12 2003.
- [19] R. R. Thomson, S. Campbell, I. J. Blewett, A. K. Kar, and D. T. Reid. Optical waveguide fabrication in z-cut lithium niobate (linbo3) using femtosecond pulses

- in the low repetition rate regime. *Applied Physics Letters*, 88(11):111109, MAR 13 2006.
- [20] G. Y. Zhou and M. Gu. Anisotropic properties of ultrafast laser-driven microexplosions in lithium niobate crystal. *Applied Physics Letters*, 87(24):241107, DEC 12 2005.
- [21] R. S. Weis and T. K. Gaylord. Lithium-niobate - summary of physical properties and crystal-structure. *Applied Physics A-Materials Science & Processing*, 37(4):191-203, 1985.
- [22] A. Barty, K. A. Nugent, D. Paganin, and A. Roberts. Quantitative optical phase microscopy. *Optics Letters*, 23(11):817-819, Jun 1 1998.
- [23] M. R. Teague. Deterministic phase retrieval - a green-function solution. *Journal of the Optical Society of America*, 73(11):1434-1441, 1983.
- [24] Weijia Yang, Peter G. Kazansky, and Yuri P. Svirko. Non-reciprocal ultrafast laser writing. *Nature Photonics*, 2(2):99-104, FEB 2008.
- [25] K. S. Youngworth and T. G. Brown. Focusing of high numerical aperture cylindrical-vector beams. *Optics Express*, 7(2):77-87, JUL 17 2000.
- [26] R. Dorn, S. Quabis, and G. Leuchs. Sharper focus for a radially polarized light beam. *Physical Review Letters*, 91(23):233901, DEC 5 2003.
- [27] Shuangyang Yang and Qiwen Zhan. Third-harmonic generation microscopy with tightly focused radial polarization. *Journal of Optics A: Pure and Applied Optics*, 10(12):125103 (6pp), 2008.

R002S94224